NextGEM

Next Generation Integrated Sensing and Analytical System for Monitoring and Assessing Radiofrequency Electromagnetic Field Exposure and Health

D3.6: Development of modelling approaches to assess internal and external exposure - Final version

Document Summary Information

Start Date	01/07/2022	**Duration**	48 months
Project URL	https://www.nextgem.eu/		
Deliverable	D3.6: Development of modelling approaches to assess internal and external exposure - Final version		
Work Package	WP3	**Task**	T3.2
Contractual due date	30/09/2024	**Actual submission date**	30/09/2024
Type	Report	**Dissemination Level**	PU-Public
Lead Beneficiary	CIMNE	**Deliverable Editor**	Eduardo Soudah (CIMNE)

This project has received funding from the European Union's Horizon Europe research and innovation programme under the Grant Agreement No 101057527

Contributors and Peer Reviewers

Contributors
Eduardo Soudah, Ruben Otin (CIMNE), Marco Spirito (TUD), Fulvio Schettino, Marco Donald Migliore (UCAS), Nikolaos Petroulakis (FORTH), Anna Laromaine, Pol Alonso (CSIC), Maarten Velghe (RIVM), Yuri Feldman (HUJI)
Peer Reviewers
Marco Spirito (TUD), Erdal Korkmaz (THUAS), Mats-Olof Mattsson (CSI)

Revision history (including peer-reviewing and quality control)

Version	Issue Date	Changes	Contributor(s)
v0.1	15/01/2024	Table of Contents provided	Eduardo Soudah (CIMNE)
v0.2	01/03/2024	Defined Task leaders	Eduardo Soudah (CIMNE)
v0.3	01/07/2024	First contributions	All involved partners
v0.4	31/07/2024	Integration and updates	Eduardo Soudah (CIMNE)
v0.5	03/09/2024	Second contributions	All involved partners
v0.7	13/09/2024	Complete version ready for peer review	Eduardo Soudah (CIMNE)
v0.8	17/09/2024	Peer review	Marco Spirito (TUD), Ruben Otin (CIMNE), Eduardo Soudah (CIMNE)
v0.9	24/09/2024	Comments addressed from peer review, technical and quality assurance.	Mats-Olof Mattsson (CSi), Nicolas Louca (eBOS), Eduardo Soudah (CIMNE), Panos Chatziadam (FORTH)
v1.0	30/09/2024	Final review and submission	Nikolaos Petroulakis (FORTH)

Disclaimer

Funded by the European Union. Views and opinions expressed are however those of the author(s) only and do not necessarily reflect those of the European Union or the European Commission. Neither the European Union nor the granting authority can be held responsible for them.

While the information contained in the documents is believed to be accurate, the authors(s) or any other participant in the NextGEM consortium make no warranty of any kind with regard to this material including, but not limited to the implied warranties of merchantability and fitness for a particular purpose.

Neither the NextGEM Consortium nor any of its members, their officers, employees, or agents shall be responsible or liable in negligence or otherwise howsoever in respect of any inaccuracy or omission herein.

Without derogating from the generality of the foregoing neither the NextGEM Consortium nor any of its members, their officers, employees, or agents shall be liable for any direct or indirect or consequential loss or damage caused by or arising from any information advice or inaccuracy or omission herein.

Copyright message

© NextGEM Consortium. This deliverable contains original unpublished work except where clearly indicated otherwise. Acknowledgement of previously published material and of the work of others has been made through appropriate citation, quotation, or both. Reproduction is authorised provided the source is acknowledged.

Table of Contents

List of Figures

List of Tables

Glossary of terms and abbreviations used

Abbreviation / Term	Description
BC	Boundary Conditions
CAD	Computer Aided Design
CEM	Computational Electromagnetics
CFD	Computational Fluid Dynamics
CST	Computer Simulation Technology (CEM commercial software)
CT	Computer Tomography
EMF	Electromagnetic Fields
ERMES	Computational electromagnetics open-source software tool
FD	Frequency Domain
FDTD	Finite Differences Time Domain
FDTD	Finite-Difference Time-Domain
FEM	Finite Element Method
FEM	Finite Element Method
FIT	Finite Integration Technique
FR1	Frequency Range 1 (frequency bands up to 7 GHz)
FR2	Frequency Range 2 (frequency bands up to 33 GHz)
HPC	High Performance Computing
IBC	Impedance Boundary Condition
ICNIRP	International Commission on Non-Ionizing Radiation Protection
IE	Inner Epidermis
IEEE/IE	Institute of Electrical and Electronics Engineers
MaMIMO	Massive Multiple Input Multiple Output
ME	Middle Epidermis
MGS	Madrid Grid Scenario
MMGS	Modified Madrid Grid Scenario
MoM	Method of Moment
MRI	Magnetic Resonance Imaging

NLM	National Library of Medicine
ORNL	Oak Ridge National Laboratory
SAR	Specific Absorption Rate
SC	Stratum Corneum
TLM	Transmission Line Matrix
UE	User Equipment
VHP	Visible Human Project
ViP / cViP	Virtual Population / Computable Virtual Population

Executive Summary

This deliverable reports on the activities of Task 3.2, "Modelling Approaches to Assess Internal and External Exposure," which is part of Work Package (WP) 3, titled "Innovative Model- and Sensor-based Technologies for Exposure Monitoring and Assessment in Human Studies." In this deliverable, D3.6, entitled "Development of Modelling Approaches to Assess Internal and External Exposure – Final Version," a comprehensive analysis of the skin model using the numerical methodologies described in D3.2 is presented.

In deliverable D3.2, we provided a detailed overview of the numerical models and approaches used to study the induced EMF generated by radiating antennas in the context of 5G telecommunication systems, both inside and outside the body. This deliverable elaborates on how the quantitative analysis and visualization of field distribution over and within the body will be conducted throughout the NextGEM project. These numerical methodologies enhance our understanding of how fields distribute in selected EMF exposure scenarios. Moreover, these approaches allow us to understand how fields couple with and are absorbed by "phantom" biological systems. The numerical approaches employed in NextGEM are based on the open-source computational tool ERMES, which has been customized for the analyses described in this report. Additionally, other commercially available tools are employed to complement the findings.

In this deliverable, we have focused on refining the simulation of skin exposure at 26 GHz, using a detailed multi-layer skin model that includes a blood vessel. This work includes detailed simulations of plane wave exposure at multiple frequencies (700 MHz, 3.5 GHz, and 26 GHz) and compares the electric field magnitude (|E|) and Specific Absorption Rate (SAR) across different skin layers. The results show that at 26 GHz, SAR values and |E| in blood vessels vary significantly depending on the orientation of the electric field relative to the blood vessel axis, with the worst-case scenario leading to SAR values of 0.39 mW/kg. Additionally, the comparison between CST and ERMES simulations has highlighted the efficiency and precision of ERMES, particularly when run on high-performance computing (HPC) clusters.

The results of this analysis will be shared with the consortium for further validation through real-life dielectric measurements using the same wave excitation conditions. These findings will guide future work on exposure assessment in 5G-related applications. This document also outlines the basics for determining sensor locations to be used in WP7 and establishes a relationship between internal and external field intensities for the scenarios addressed in Task 3.4. Furthermore, the analyses carried out in Task 3.2 will serve as inputs for the biological experiments in WP4 and WP7.

1 Introduction

Numerical codes have grown to become invaluable tools for the study of electromagnetic fields, enabling researchers and engineers to gain profound insights into the behavior of these fields in diverse scenarios and their interactions with different types of matter. The profound changes in wireless communication technologies, in the 5th and forecasted 6th generation, in both carrier frequency and signal envelope, have presented complex challenges in understanding the propagation of such (rapidly time-varying) signals and measuring the intensities of EMF in complex environments, i.e., urban and indoor. This technological development has led to open questions on the possible impact of these fields on biological systems and, especially, on humans. Consequently, the utilization of numerical codes has become increasingly important in comprehending and optimizing these cutting-edge as well as wide-spread technologies. Furthermore, numerical simulations provide a visual representation of complex EMF interactions, offering intuitive insights into the fields' behavior, and enabling researchers to make data-driven decisions in designing advanced wireless systems.

The significance of employing numerical codes for the study of 5G and 6G technologies lies in their ability to accurately model and analyze complex electromagnetic phenomena. With the proliferation of wireless devices and the ever-growing demand for data transmission rates, the investigation of EMF characteristics at higher frequencies has become crucial. Numerical codes offer a versatile and efficient way to simulate and predict the behavior of EMF in different exposure scenarios, enabling researchers to optimize system designs, assess the exposure levels in different use cases, and ensure compliance with safety standards. Improvements in numerical models for real EMF exposure scenario simulations are part of the NextGEM project's objectives. This document aims to provide a technical background of the numerical models used during the NextGEM project and define various real scenarios for study and analysis. By enhancing the accuracy and capabilities of these numerical codes, the NextGEM project strives to advance our understanding and quantification of EMF in evolving wireless communication technologies.

1.1 Mapping NextGEM Outputs

The purpose of this section is to map NextGEM 's Grant Agreement (GA) commitments within the formal task description and deliverables against the project's respective outputs and work performed.

Table 1: Adherence to NextGEM's GA Tasks and Deliverables Descriptions

TASKS	
Task Number & Title	**Respective extract from formal Task Description**
Task 3.2 - Modelling approaches to assess internal and external exposure.	The main scope of this task is the numerical modelling of the EMF generated by radiating antennas and the induced EMF inside the human and C. elegans bodies. Numerical simulations provide a clear visualization of the fields inside a body which will help in understanding field distributions relative to different organs and parts of the body. This task will develop novel open-source computational tools able to carry out such analysis and will make possible the coupling between the external EMFs and the fields inside human and animal bodies complemented with multiphysics modelling of the coupling of EMF with thermal and CFD physics if needed. Results will be applied to a skin model based on CST for studies of EMF exposure in different frequency bands.
DELIVERABLE	
Deliverable: D3.6: Development of modelling approaches to assess internal and external exposure - Final version (M27) This deliverable will provide insight into how external EMF in a 5G environment translates into induced electric field distribution in different parts of the human and the nematode body.	

1.2 Deliverable overview and report structure

This deliverable aims to explain the numerical models and tools for monitoring and assessing the exposure and health effects of radiofrequency electromagnetic fields (EMFs) in the context of 5G and 6G technologies. The deliverable provides an overview of the following aspects.

Based on the objectives and work carried out under Task 3.2, the document starts with the Executive Summary followed by the introduction of the document in Section 1.

Section 2 includes the simulation approaches for different scenarios and frequencies, such as whole-body exposure, local exposure, and surface-based modelling.

Section 3 defines the geometric models used to represent the physical structures in the simulations, such as volumetric models and surface models of the human body, skin, and *C. elegans*.

Section 4 provides the numerical tools for EMF analysis, such as the open-source finite element code ERMES, which has been customized according to the project requirements and it will also be integrated into the NIKH platform.

Section 5 presents the preliminary examples of the models and simulations for various use cases and challenges, such as the FR1 and FR2 ranges and the Impedance Boundary Conditions (IBC). New to this section is the study of a human skin model, utilizing an open-ended coaxial probe to conduct preliminary tests on the dielectric properties of biological tissues. The final measurement will be analyzed and compared in case study 3. This non-destructive technique was applied specifically to the skin model, allowing for accurate characterization of electromagnetic behavior at both FR1 and FR2 frequencies. The results from these measurements provide further validation of the electromagnetic properties of the skin model and offer insights into surface-level EMF interactions at high frequencies.

Finally, Section 6 concludes the deliverable.

1.3 Updates from previous Deliverable D3.2 "Development of Modelling Approaches to Assess Internal and External Exposure – Initial Version"

This deliverable is a continuation and an update of the computational tools used for numerical simulation of the electromagnetic field. Apart from the updated content in all sections, the main enhancements to this deliverable can be summarized as follows:

- Section 5.1.2: A comprehensive analysis of a skin model in the FR1 range was conducted. The electromagnetic properties of different skin layers were identified and characterized at 700 MHz and 3.5 GHz.
- Section 5.2.1: A detailed analysis of a skin model in the FR2 range was performed, focusing on the electromagnetic properties of various skin layers at 26 GHz.
- Section 5.2.2: A cross-validation between ERMES and CST Studio was carried out.
- Section 5.2.3: A numerical simulation of the coaxial test was completed.

2 EMF simulation approaches

EMF exposure limits define the maximum allowable levels of electromagnetic radiation that humans can be exposed to without adverse health effects. These limits are crucial for ensuring safety in various contexts, including occupational settings, public environments, and medical applications. During the NextGEM project, computational models will be used to understand the interplay between the radiation sources and the exposure, especially the effects in humans due to mobile phones and base stations operating in the 5th generation communication systems.

The regulatory actors provide guidelines for exposure limits based on scientific evidence. The ICNIRP Guidelines for high frequency electromagnetic fields (EMF), which globally are the most used, focus on limiting exposure in order to protect humans to (EMFs) in the range of 100 kHz to 300 GHz [1]. The basic restrictions limits are divided into two main categories, whole body and local exposure, depending on the specific scenario, while the reference levels are specific for whole-body exposure. For the basic restriction, the usage of the whole body or local exposure will depend on the context and scenario where the electromagnetic field propagates; as an example, the exposure generated by a user equipment (UE), like a mobile phone, will fall in the category being characterized by the local exposure since its field is confined to limited portions of the body. Differently, when the exposure is generated by a remote source located far away from the user, the whole body is under investigation. Both scenarios will be covered during the NextGEM project; local exposure, which is Case Study 1, and whole-body exposure, which are Case Study 2 and 3. The wording "local" or "whole-body", which are terms used to define the area of a person exposed to the field, should not be used as a synonym of "far-field" and "near-field", which are terms used to define the relative distance to the source radiating element and are depended on characteristics like frequency and size of the radiator. For instance, there may be instances where the exposure is confined to a specific area (local exposure) despite the scenario being situated in the far-field region of the source. Alternatively, the exposure might encompass the entire body (whole-body exposure) even when the distance to the source aligns with the near field of the radiating element.

2.1 Whole body exposure in complex environments

When the radiation generated by the source involves the whole exposed object of investigation, whole body basic restrictions or reference levels, as defined in [1] apply. It could happen, but it is not a rule that the source of the field is located at an electrically large distance (a large number of wavelengths of distance) from the point where the EMF is evaluated (the observation point). In these cases, to evaluate the exposure, methodologies based on ray-tracing are the most suitable.

Ray-tracing approaches employ discrete rays to represent the wavefronts as they propagate from a transmitter through a given environment. Rays interact with geometries in the scene through reflections, diffractions, and transmissions. Rays that reach a given observation point are the results of the various paths that waves may travel from the transmitter to that point. The exposure quantities can be calculated through the superposition of the contributions from all of the propagating waves that reach that receiver point.

Simulations based on ray tracing techniques considered in the NextGEM project are defined and studied in Task 3.4. In this task, simulations will be performed for both the outdoor environment and the indoor environment. Of relevance to the outdoor environment, two typologies of 3D scenarios are considered:

- A simplified scenario: based on the Madrid Grid Scenario (MGS) [2], including some variations for the heights of the buildings, named Modified Madrid Grid Scenario (MMGS).
- A real town scenario: as chosen by each partner, including the orography.

The MMGS consists of an ordered and regular distribution of buildings and open areas, separated by regularly distributed streets. The whole scenario is generated by orderly placing a basic element side to side, a so-called tile.

Each tile consists of a 387 m by 552 m area, including a sidewalk, parking lane and road lane. Within the scenario, there are two shapes of buildings, namely the square and rectangular base buildings; there is an open area representing a square; each element is separated from the other by regularly distributed streets. The original MGS defines the height of each building according to a fixed number of floors; each floor is 3.5 m high. Differently from the MGS, in the MMGS, the number of floors for each building varies randomly. The analysis of the scenario allows us to consider the influence of the materials' behavior in the calculation of the radio coverage and the main processes of electromagnetic interaction because the electromagnetic properties of the different representative materials are considered for each element of the scenario. For an FR1 scenario, the selected size is currently 3km

x 3km. For the FR2 scenario, the basic tile is the same MMGS as for FR1; the size of the whole FR2 scenario is currently in the definition phase.

The 3D representation of the scenario can be performed by using different techniques, such as stereoscopic aero photogrammetry. The stereoscopic reconstruction process allows the fusion of two or more different bidimensional images into a single three-dimensional view; it is based on the physiological principle of the three-dimensionality perception in human vision. Within the reconstructed model of a real town, all the characteristic elements of the city are represented with high precision; the orography is represented; surrounding environments, like hills or mountains, rivers and green areas, are included, too. The randomness of the real environment and geographical characteristics are fundamental for determining the field distribution; each element present in the real town is reconstructed through a specific object with its own characteristics, size, and electromagnetic properties of the materials to allow a complete evaluation and realistic evaluation. The realism is apparent in Figure 1, which shows the Modified Madrid Grid Scenario and the Real Town scenario, where, e.g., hills in the landscape are clearly shown.

Indoor propagation will also be explored for specific scenarios both at FR1 and FR2. Now, the scenario is under discussion in Task 3.4; an example of a possible indoor scenario and coverage in shown in Figure 1c.

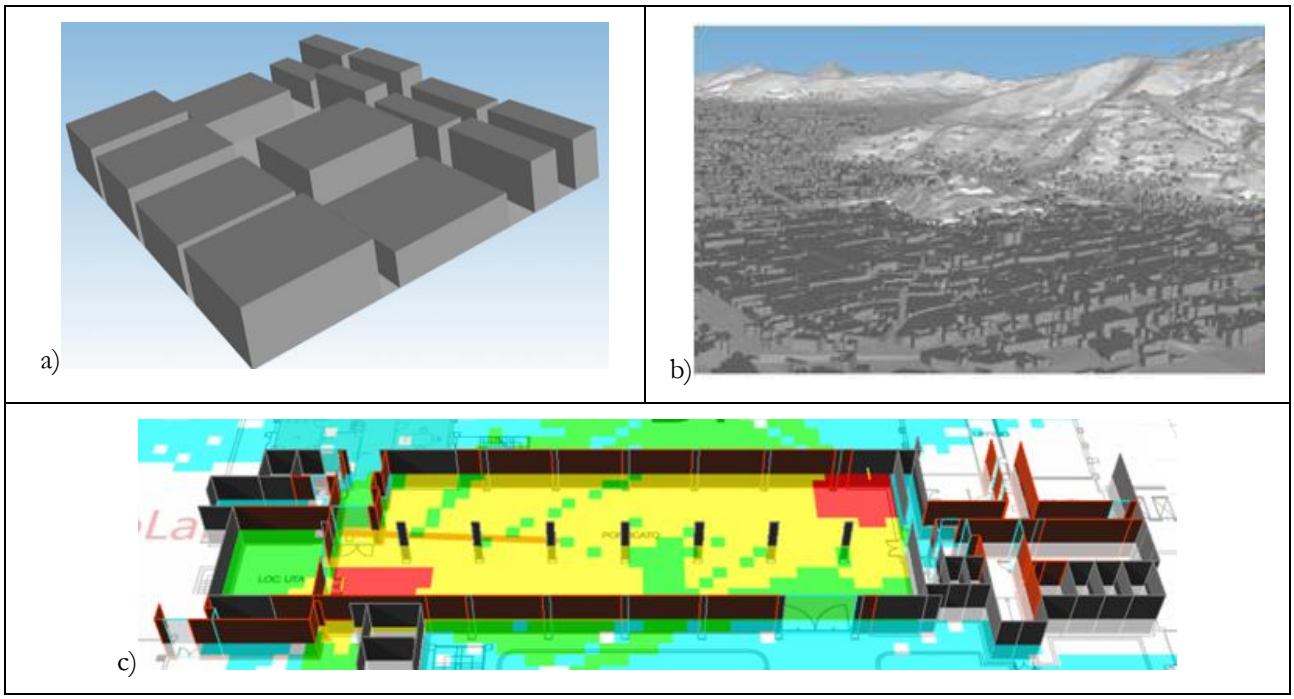

Figure 1: Basic tile of MMGS (a). Example of real scenario representation (b). Example of an indoor scenario (c).

2.2 Local exposure

Local exposure to EMF in humans refers to the exposure of specific parts of the body to EMF. For an efficient evaluation of the local exposure in terms of SAR, according to the requirement of exposure guidelines [1], a comprehensive evaluation of all electromagnetic field components and the domain is needed. If the exposure takes place within the near-field region of the source, it is necessary to consider all electromagnetic field components and assess the influence that the radiated object has on the source itself. This entails considering not only the geometry of the radiating components of the source but also the precise details of the relative position between the source and the radiated object, considering factors such as shapes and materials. Any change introduced in the scenario implies a re-evaluation of the problem since boundary condition changes and, consequently, the exposure. In this case, separation between the exposed object and the source is not applicable, and the electromagnetic problem shall be solved by a full wave approach. If the assessment of local exposure is based on SAR, it will be necessary to appropriately average it over volumes or surfaces. In the NextGEM project, we will utilize the open-source ERMES code, which has been developed by CIMNE. ERMES [3] solves the full-wave Maxwell's equations in the frequency domain, describing how the EMF propagates, and can provide a detailed spatial distribution of the SAR within a human body model (see Section 4.1 and Figure 2 and Figure 3).

Figure 2: Example of head exposure to a radiating element [3]: geometry (a), meshing in the simulator environment (b) and resulting SAR inside the body (highest SAR in red, lowest in blue) (c).

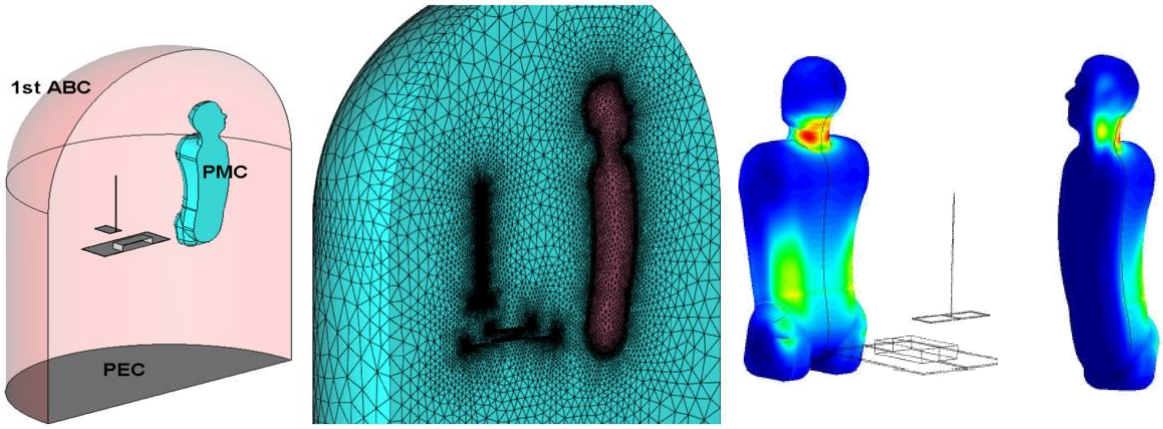

Figure 3: Example of upper torso exposed by a PMR unit [3]: geometry (a), meshing in the simulator environment (b) and resulting SAR inside the body (highest SAR in red, lowest in blue) (c).

3 CAD Models

In computational electromagnetic simulations, the choice of geometric models is crucial for accurately representing the physical structures under investigation. These models help define the boundaries, shapes, and materials within the simulation domain. There are generally two main types of geometric models used: volumetric models and surface models.

- Volumetric models are crucial for studying how electromagnetic fields penetrate and interact with the interior of complex structures, such as biological tissues or composite materials. They are computationally intensive but offer high accuracy. Volumetric models represent the entire volume of the object under study, and they are particularly useful when dealing with complex, three-dimensional structures. Volumetric models are used when you need to simulate how electromagnetic fields propagate through and interact with the interior of objects. For example, in a full-body simulation for computational electromagnetic purposes, each organ and tissue type within the body would be represented as a distinct volume with defined electromagnetic properties.
- Surface models, on the other hand, represent only the outer boundaries or surfaces of 3D objects. Surface models are often used when the details of the interior of the object are not of primary interest or when the object's complexity can be sufficiently captured by its external geometry. Surface models are employed when it is only required to analyse the interaction of electromagnetic fields with the exterior of objects or surfaces. They are suitable for scenarios where the behaviour of electromagnetic waves at the boundaries is the primary focus. For example, in a full-body simulation using a surface model, the human body would be represented as an outer shell, with distinct surfaces representing different tissue types. This is less computationally intensive than a volumetric model and is suitable for applications where interior details are not essential because the fields do not penetrate the body.

The choice of geometrical models in electromagnetic field simulations depends on the specific requirements of the study, the complexity of the structures being analysed, the operational frequency and the computational resources available.

3.1 Full body volumetric models

Volumetric models come into play when we are analysing electromagnetic fields (EMF) that penetrate the human body, especially at frequencies below a few gigahertz (GHz). These models become essential when our central objective revolves around evaluating crucial parameters such as the dispersion of EMF power within internal organs and the spatial distribution of the SAR. The Specific Absorption Rate (SAR) is the energy deposited into the tissues by the EMFs inside the body per unit mass, and it is measured in watts per kilogram. SAR is important for assessing the potential health risks of exposure to electromagnetic fields. In essence, volumetric models are the preferred approach for acquiring a deep understanding of how EMF interacts with and impacts complex structures. organs and tissues within the body. This knowledge is invaluable for a wide range of applications, spanning from the assessment of medical device safety to the enhancement of wireless communication technologies. Figure 4 shows a representation of the human body at different volumetric levels.

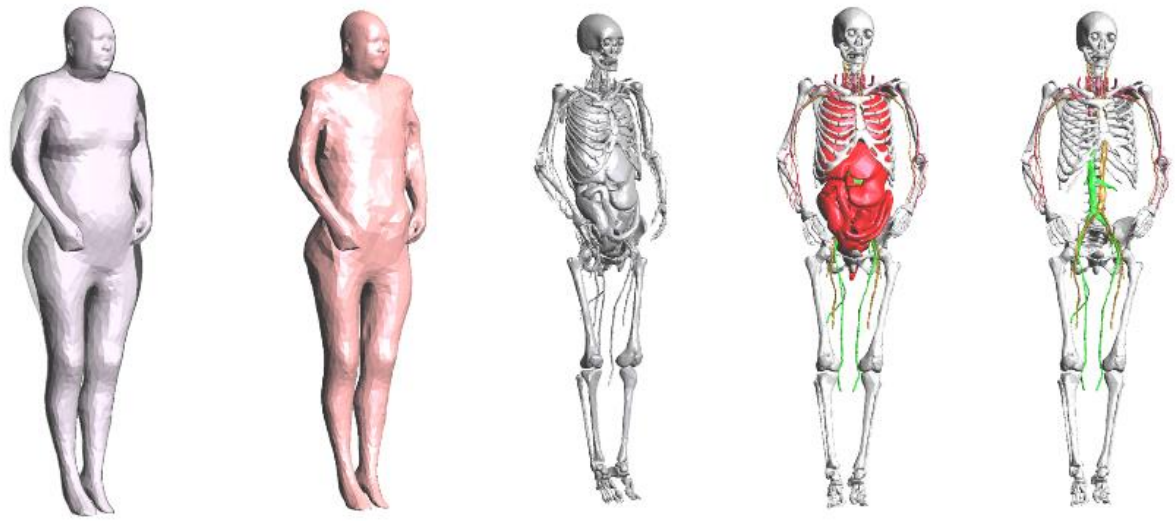

Figure 4: Volumetric parts of a full body.

Evaluating the field distribution inside the human body is crucial, especially when electromagnetic devices are being developed, for the assessment of the potential health risks of exposure to electromagnetic fields. Unfortunately, there are huge limitations on the direct measurement of the electromagnetic field inside the tissues and organs of living organisms. A possible approach relies on the use of the Specific Anthropomorphic Mannequin (SAM) phantom, which is filled with homogeneous, dispersive material in order to perform SAR measurements, according to IEC 62209-1528:2020 [4]. Even if compliant to the standards, such phantom models remain relatively simple and are usually used to assess conservative exposure.

As a result of the rapid development of computer science, simulations on the human body models can be performed to predict the electromagnetic radiation effects, as well as heating and SAR distribution. Nowadays, the development of computational human models used for a variety of applications is still in focus. With the ever-improving computer graphics and medical techniques, more accurate computational human body models are being developed. The voxel-based human models, also known as tomographic models or voxel phantoms, can be created by analogue photography of slices of a frozen body. However, in most cases, the voxel-based human models are built from highly accurate cross-sectional images of internal organs obtained using computer tomography (CT) and magnetic resonance imaging (MRI) devices. Once a dataset from the medical scans is available, a process of segmentation is conducted to identify the organs and the tissues in the human body. The models are then segmented (from the pixel data from these 2D images, transformed in three-dimensional volume elements called voxels).

At the end of the process, a phantom is created to be further used in simulation software numerically solving Maxwell's equations, such as time-domain solvers (finite integration technique solvers (FIT) or finite-difference solvers (FDTD), frequency-domain solvers (finite element method (FEM) or method of moment (MoM)) or Monte-Carlo ionizing radiation simulators. These models have a very large application range in the simulations of realistic electromagnetic problems, the main goal being the computation of electromagnetic fields inside and outside the voxel-based human body for dosimetry calculations.

The initial generation of computational human models, developed from the 1960s to the 1980s, primarily utilized basic geometrical shapes. Examples of these models were created by the Oak Ridge National Laboratory (ORNL) [5][6], featuring head, neck, torso, and leg components. Internal organs were represented using equations of ellipsoids, cylinders, spheres, and cones positioned within the torso. Despite aligning with the International Commission on Radiological Protection's "Reference Man" [7] dimensions, the simplicity of organ shapes and their placement in an elliptical cylinder torso deviated from the realistic anatomical structures and positions in the human body.

Since then, huge steps forward have been made in the modelling, taking the pixel data from the images as a starting point, as mentioned above. Two types of widely used computational models were created: surface-based and voxel-based human models. The surface-based human models (see Section 3.2) are built from triangular surface meshes, which are used to represent the tissues in the human body. The surface meshes will be extracted directly from the voxel meshes. They can approximate the outer surfaces and shapes of the organs and tissues of the human body in detail. These models are widely used in the computer graphics domain. A very popular surface model family is the Virtual Population (ViP 3.0[1]) [8]. This model family elevates computational simulations in 3D anatomies to an unprecedented level of detail and accuracy with more than 300 tissues and organs per model and a resolution of $0.5 \times 0.5 \times 0.5$ mm³ throughout the entire body. An evolution, named Computable Virtual Population V4-0 and V3-x (cViP) models, is currently under development and includes more than 120 anatomical features and more than 1000 separate tissue regions (V4-0), with about 240 peripheral nerve structures.

Another example of a surface model was generated using the open-source high-resolution cryosection image dataset from the National Library of Medicine (NLM) Visible Human Project (VHP)[2]. The Visible Man data set was publicly released in 1994, and the Visible Woman in 1995. This Project included digitized photographic images from cryo-sectioning, digital images derived from computerized tomography, and digital magnetic resonance images of two cadavers. Even today, the corresponding cryosection images (24 bits of colour, pixel resolution of 0.33 mm) provide state-of-the-art resolution of muscles, other soft tissues as well as bones.

The voxel-based human models are also known as tomographic models or voxel phantoms. They are generated from 2D cross-sectional images from medical scans, such that the pixel data are transformed in three-dimensional

[1] Currently, version ViP 3.1 is available at https://itis.swiss/virtual-population/virtual-population/overview/

[2] https://www.nlm.nih.gov/research/visible/visible_human.html

volume elements called voxels. Each voxel can be a cube or a parallelepiped and is filled with one material assigned with an ID number, which represents a particular tissue or organ.

Both types of human models have advantages and disadvantages. On one hand, the surface-based models can be used with numerous simulation methods. On the other hand, the voxel-based models can be used with FDTD solvers and Monte-Carlo ionizing radiation simulators (or other similar software), which are based on rectangular grids. Nevertheless, the voxel-based models can easily map highly inhomogeneous tissue distributions. The surface-based models, which include many tissues and organs, are described by large-sized triangular surface meshes, which limits their usage only in FDTD solvers. A further advantage of surface-based models is their ability to describe curved organs realistically. The main advantage of voxel models is the possibility of being scaled in order to fit the dimensions of the studied human models, so they can be both increased or decreased in size. Despite their many positive characteristics, the voxel-human models also have some drawbacks. The first one is the voxel shape: the representation of the human model using voxels gives a staircase surface rather than a smooth one. This could lead to an overestimation of the size of certain organs. Another drawback is the problem related to the segmentation of tissues with dimensions smaller than the voxels' dimensions. In some cases, this could lead to inaccurate simulation results. The voxel model dataset is stored in a large data file. The content of such a file is not prescribed by a standard. Most of these files consist of a header of different size and a body in which the voxel values are stored. Also, there is no prescribed format for the type of the file: the voxel file is usually written in a binary format but can also be written in ASCII format.

According to [9], in 2017 there were 34 whole body models listed worldwide, mostly voxel-based, which vary in age, sex, dimension and weight. Among them, within NextGEM project, the CST Voxel family will be used. The CST Voxel Family is a group of eight human model voxel data sets created from eight persons of different gender, age, and stature (see Figure 5), included in the CST Studio Suite® (https://www.3ds.com/) installation. In particular, Hugo is based on VHP, has a height of 187 cm and a mass of 113 kg, and is available in 1-, 2- and 5-mm resolution. The 1 mm version is the most detailed and also includes different types of tissue and air inside the body. A useful feature of these models, as well as of many models reported in [9], is that they are posable; that is, they can be put into different postures like walking, sitting, or holding devices. This will allow to more realistically model the scenarios that will be simulated.

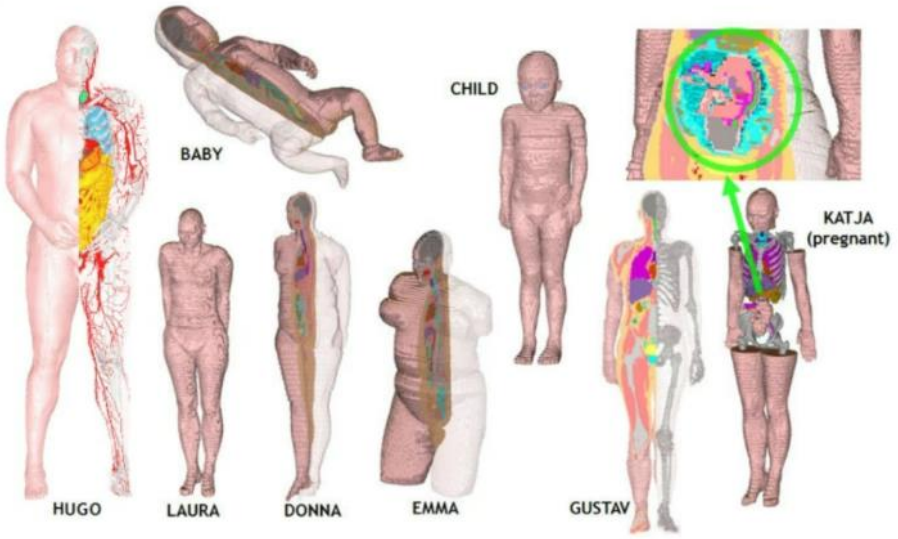

Figure 5: The CST voxel family.

3.2 Surface models

In the high-frequency range (typically above tenths of GHz), the electromagnetic fields do not penetrate the human body significantly. This allows a different modelling approach, focusing on the surface rather than the entire volume of the body. Surface-based modelling is particularly useful when the primary concern is to understand how EMFs interact with the outer layers of the body, such as the skin. At these frequencies, the electromagnetic energy is absorbed and dissipated primarily at the body's surface. Through the surface-based modelling approach, internal parameters of interest, such as the average SAR, can be calculated by analysing the fields at the surface. The SAR represents the rate at which electromagnetic energy is absorbed by biological tissues. By obtaining SAR and other

relevant internal magnitudes from the fields at the surface, researchers can assess the potential health effects of EMF exposure and ensure compliance with safety standards.

Surface meshing in computational electromagnetics often involves the use of triangles or quadrilaterals (Figure 6). The resolution of the mesh (i.e., the number of cells or elements) depends on the specific requirements of the simulation. For instance, in areas where there is a rapid change in the electromagnetic field, it is recommended to have a fine mesh (i.e., a small surface of each of the triangles or quadrilaterals) to minimize the effect of change in field variables. Furthermore, in terms of computational efficiency, surface-based modelling can be more efficient than volumetric (or voxel) modelling because it focuses on the surface where the EMFs predominantly interact. This can significantly reduce the number of cells or elements needed to resolve the geometry, thereby reducing the computational resources required. However, the exact benefits in terms of computation time and accuracy would need to be quantified based on the specific application and simulation requirements. For example, the position, size, and sex of the human body related to EMF is that they can affect the EMFs, for example, in case of a pregnant woman (Figure 7). In deliverable D3.6, we will focus on this aspect.

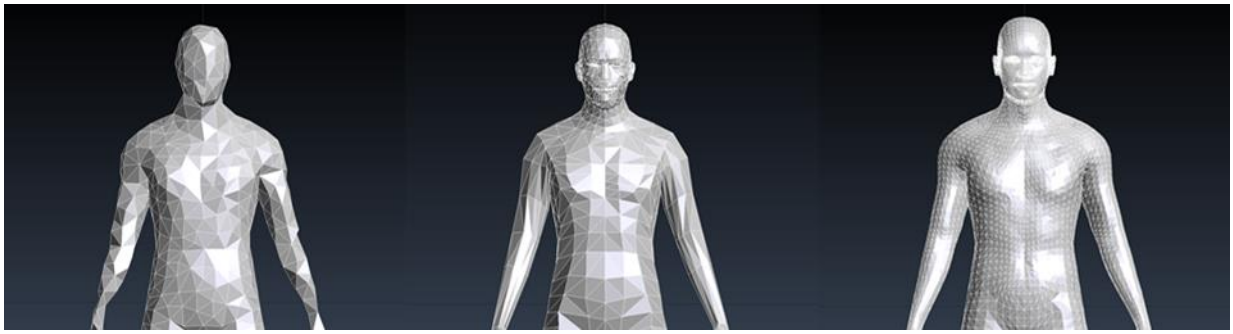

Figure 6: Surface mesh discretization for a human body

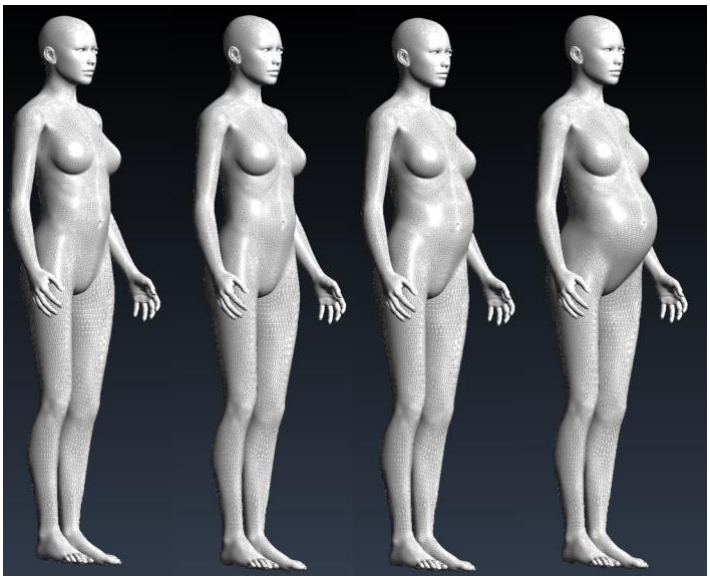

Figure 7: Women at various stages of pregnancy.

In summary, the combination of volume and surface meshing in computational electromagnetics offers a comprehensive solution for studying electromagnetic interactions both within the volume and at the surface of complex geometries. The choice between volume and surface meshing depends on the simulation objectives, the nature of the electromagnetic interactions, and the desired level of detail in representing the geometry. In Figure 8, we present a snapshot of the computational setup, highlighting the distinction between volume and surface meshing in the context of computational electromagnetics. This figure provides a visual insight into how the geometry is discretized for electromagnetic simulations. The volumetric mesh encapsulates the entire space surrounding the human body. This meshing strategy involves dividing the three-dimensional volume into small, interconnected elements, commonly referred to as voxels, as explained previously. The surface mesh is employed to specifically model the exterior boundaries of the body. The surface mesh is adept at capturing the intricate details of the body's contours, making it suitable for scenarios where electromagnetic interactions predominantly occur at the surface, such as in high-frequency regimes.

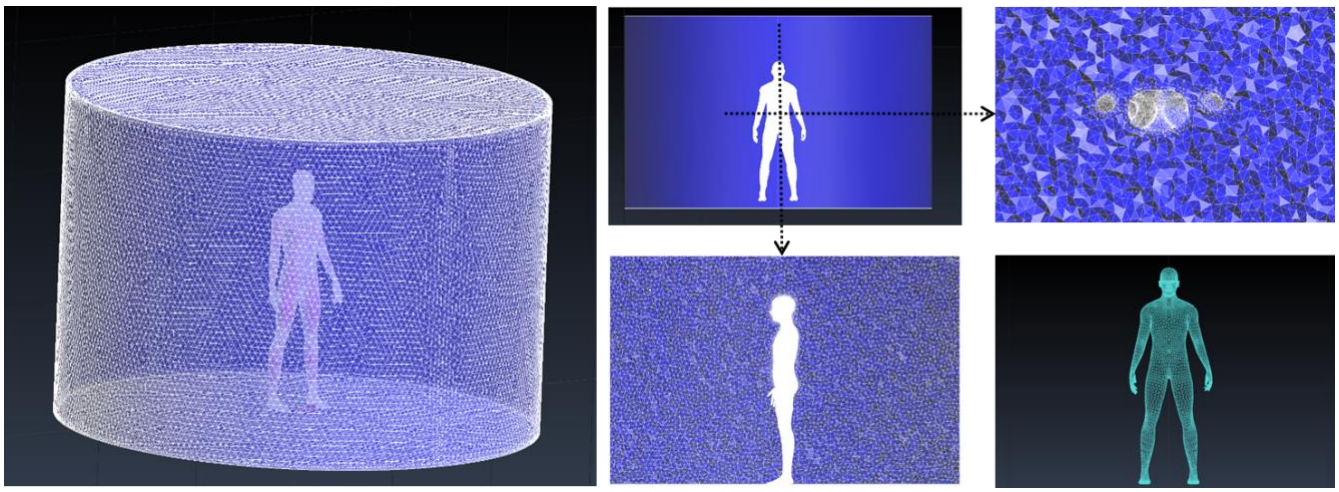

Figure 8: Representation of a human body(surface) inside a volume mesh. Cross-sectional planes of the human body are inside the volume. Human surface body.

3.2.1 Tissue computational models

As mentioned in the previous sections, at higher frequencies (i.e., tens of GHz) EMFs do not penetrate the human body significantly. In these conditions and when the complexity of the phantom requires it, surface models can be employed. In order to evaluate the impedance these surfaces need to provide, an understanding of how the outer layer of the body (i.e., outer skin layer) responds to electromagnetic waves is required. In order to carry out this task and provide an accurate "impedance" level to the surface the NextGEM project will employ a special model of the skin previously developed by one of the partners.

This state-of-the-art model is realized, accounting for four-layered unit cells, which were developed using the CST MICROWAVE STUDIO® software. The model has two main layers: the dermis and the epidermis, as seen in Figure 9. The epidermis can be roughly divided into three basic sub-layers: inner epidermis, middle epidermis, and Stratum Corneum (SC), going from the deepest to the most superficial.

Millimeter wave radiation typically does not penetrate beyond the depth of the epidermis. Therefore, only the coil duct section of the whole sweat gland duct component is considered. In addition, FR1 and FR2 frequency bands typically do not penetrate beyond the dermis. Therefore, the hypodermis has no important role in shaping the EM spectral response and is not included in the model. Each unit cell contains one helically shaped sweat gland duct embedded into the epidermis (see right-hand side of Figure 9) to correspond with the position of the duct noted by optical coherence tomography (Figure 10). The boundary between the epidermis and the dermis can be regarded as a reflection plane due to the difference between the dielectric properties of the respective layers (as shown in Figure 12). This boundary was modelled as a two-dimensional (2-D) sinusoidal surface, which corresponds to the papillary dermis of the human skin.

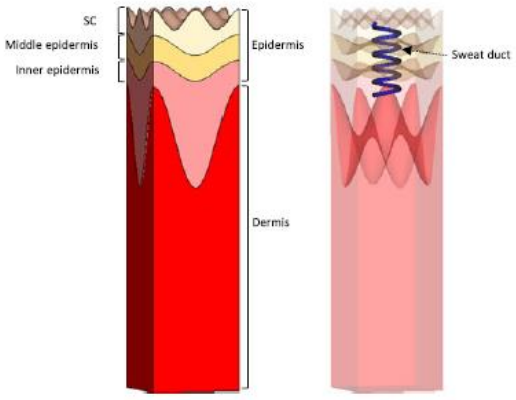

Figure 9: Skin model. On the left: unit cell, consist of two main layers; dermis and epidermis. The epidermis is here described as consisting of three sublayers: Inner Epidermis (IE), Middle Epidermis (ME), and Stratum Corneum (SC).

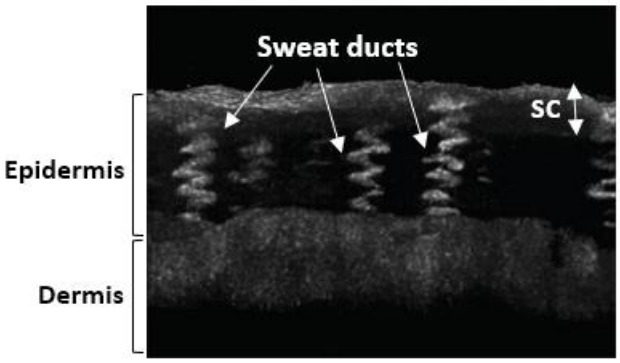

Figure 10: Optical coherence tomography image of a human sweat gland duct in vivo. The coiled portion of the ducts are clearly visible.

The dielectric permittivity of each layer of the model, described in Table Table 2, can be computed by extracting the water concentration profile of that given layer, as shown in Figure 11, and using the mixture formula presented in [10].

$$\varepsilon_{\text{layer}} = \varepsilon^{bm} \frac{\left(2\varepsilon^{bm} + \varepsilon^{w}\right) + 2\phi\left(\varepsilon^{bm} - \varepsilon^{w}\right)}{\left(2\varepsilon^{bm} + \varepsilon^{w}\right) + \phi\left(\varepsilon^{bm} - \varepsilon^{w}\right)}$$

where ε^{bm} is the permittivity of the dry biological structural components, approximately 2.2, ε^{w} is the permittivity of water, and φ is the volume fraction of the water component [10].

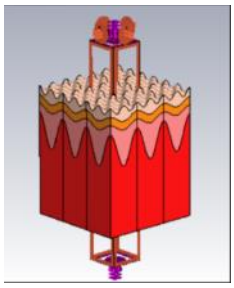

Figure 11: Skin model of Figure 8 with applied periodic boundary conditions.

The proposed model can then be used to compute the surface impedance by using in CST periodic boundary conditions, where the unit cell shown in Table 2, as shown in Figure 11, realizing a continuous skin tissue phantom.

Table 2: Estimated skin dielectric permittivity and ac conductivity, which were used in the simulations model. The ac conductivity of the sweat gland ducts is considered to be much higher than that of its surrounding epidermis.

Component	Relative Permittivity	AC Conductivity (S/m)
Dermis	3.8	30
Deep epidermis (E_1)	3.7	1
Middle epidermis (E_2)	3.2	0.5
SC (E_3)	2.7	0.00001
Sweat gland duct	5	100-10,000

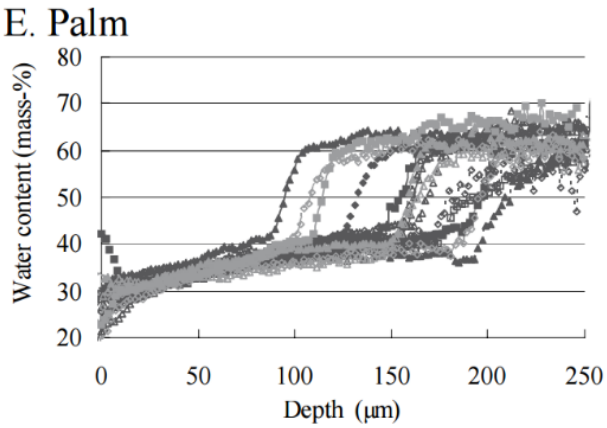

Figure 12: Epidermis water concentration profile as a function of the depth of palm skin. Those measurements were made in vivo, where Raman spectra were obtained at different depths below the skin surface using a confocal Raman spectrometer (Reproduced from Egawa et al. (2007).

3.3 C. elegans models.

C. elegans is a 1 mm long nematode featuring four larval stages and one adult stage, altogether constituting a fast life cycle of approximately three weeks. Despite its small size, it has a differentiated muscle wall and distinct reproductive, digestive, and nervous systems. Of those, the digestive system and the eggs are easily visible in the microscope due to the transparency of their cuticle, which is analogous to the human skin. These characteristics make *C. elegans* suitable for modelling EMF absorption rates, focusing either on the whole nematode body as well as on particular areas (i.e., the eggs), requiring, due to the small size and the relatively simple shape of the organism, less computational power than modelling the same parameters in higher organisms.

The Virtual Worm Project (http://caltech.wormbase.org/virtualworm/) recreates the nematode *C. elegans* in virtual form using the open-source 3D content creation suite Blender. The 3D models are based on the depictions of *C. elegans* anatomy found in Worm Atlas, Mind of the Worm, and the Worm Image repository (Figure 13). The Virtual Worm Browser is currently under development, but it will allow us to explore the anatomy of *C. elegans* during NextGEM project.

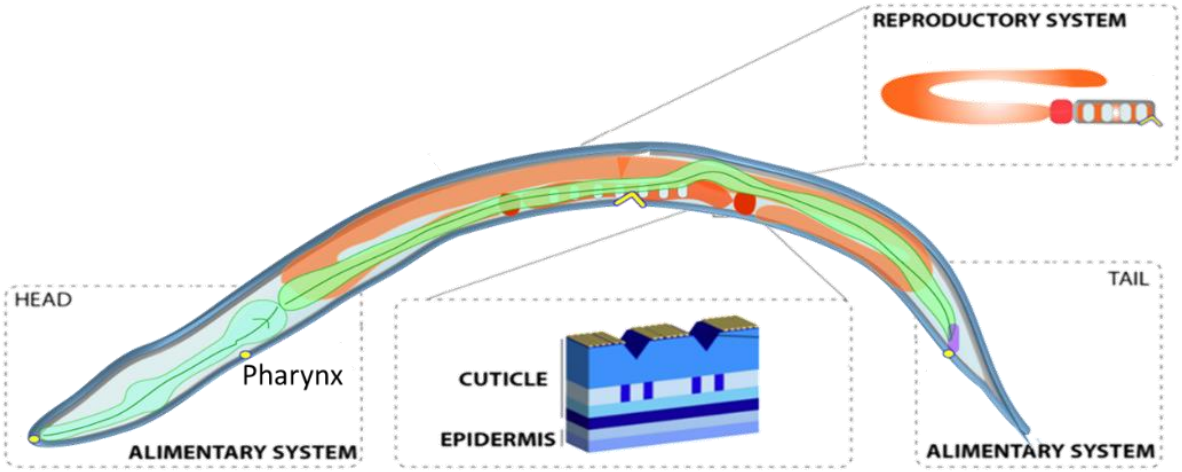

Figure 13: Anatomical scheme of the *C. elegans* and its main organ systems with exception of the nervous system [11]

4 Numerical tools for EMF analysis

There are several numerical techniques available to analyse electromagnetic problems [2][3][12]. In Figure 13from reference [2] a summary of the most common computational methods is shown. In Deliverable D2.2 there is a description of statistical, deterministic, and numerical methods (FDTD, FEM, FIT, MoM) used for computational electromagnetics.

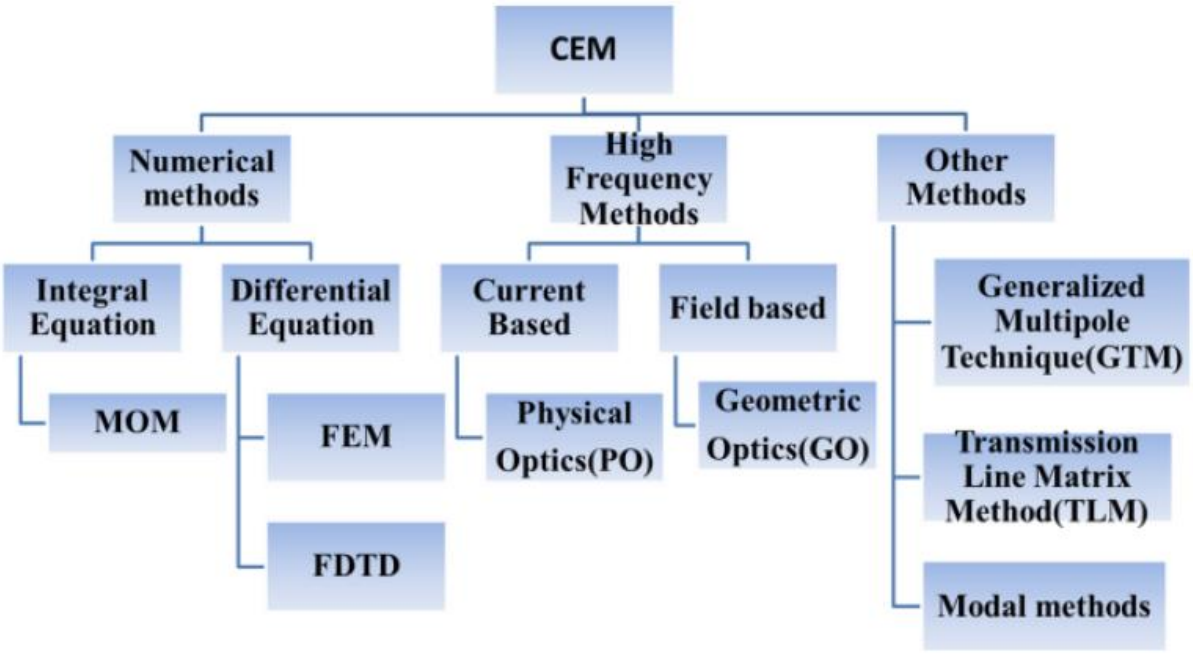

Figure 14: Computational electromagnetic numerical methods

For the NextGEM project, the main approaches of interest are the high frequency methods (PO, GO) for computing EMF when the wavelengths are much smaller than the dimension of the problem domain ($\lambda << D$), as in the examples of Section 2.1, and the Finite Element Method (FEM) in Frequency Domain (FD), for computing EMF when $\lambda \leq D$ and we have complex materials properties and geometries, as in the examples of Section 2.2. We chose FEM-FD because its superiority when dealing with complex geometries and materials properties as well as its efficiency when solving a small number of single frequencies.

Other common approaches, such as the Finite Difference Time Domain (FDTD) method or the Method of Moments (MoM), are also very powerful, but they present some limitations for the NextGEM project. For instance, the FDTD method requires a box-like discretization, which can induce modelling errors on curved geometries and difficulties when defining the material properties on the material interfaces. Moreover, for a single frequency, it is necessary to solve all the transients before reaching the stationary state and the time steps must be small enough to satisfy the proper stability condition. On the other hand, with another common approach as MoM, a surface integral method, we can efficiently solve single frequencies and curved interfaces in open domains. A further problem with MoM is that it can be computationally very expensive when solving volumetric dielectric materials as the ones of interest for NextGEM project.

There are several commercial tools available to implement the above methods (e.g., SEMCAD X, CST, HFSS, FEKO), and some of these tools will be used in NextGEM when needed. Nevertheless, they often present limitations in modelling capabilities, availability, and computational performance. Hence, to overcome these difficulties and fill the gaps in the commercial software, we will customize the open-source computational tool ERMES [13] for the specific needs of NextGEM. We will add new boundary conditions and new modelling features and improve its High-Performance Computing (HPC) capabilities. New numerical algorithms will be tested and validated to improve numerical efficiency and accuracy, and new interfaces (ray-tracing with full-wave EM solver) and modelling capabilities (coupling EM with other physical models) will be developed, further advancing EMF modelling in complex environments. At the end of the project, all these new developments will be made freely available to the general public.

4.1 Open-source finite element code ERMES

ERMES is an open-source finite element code in the frequency domain designed to solve electromagnetic problems. It implements in C++ several FEM formulations (weighted regularized Maxwell equation method [14][15] edge elements method [16], local L2 projection method [17]) with nodal and edge elements of 1st and 2nd order for the electric field and the magnetic vector potential. We can select the most stable formulation for each problem and the one that produces the best conditioned matrix to be solved efficiently with low-memory consuming iterative methods. The range of available formulations makes ERMES a versatile tool which allows us to solve a wide variety of electromagnetic problems (e.g., microwave engineering [14], bio-electromagnetics [15][18], electromagnetic compatibility [19] electromagnetic forming [20], and nuclear fusion engineering [21]). It's noteworthy that, unlike certain commercial codes such as CST, which predominantly relies on Time Domain (TD) techniques like FIT and Transmission Line Matrix (TLM) methods, ERMES excels in the Frequency Domain (FD). This distinction becomes pivotal, especially when addressing scenarios involving a reduced number of frequencies, as evident in the NextGEM project. Time domain methods necessitate the resolution of transients before attaining a stationary state, often demanding more computational time. In contrast, Frequency Domain (FD) methods champion efficiency by solving one frequency in a single step. Comparisons between the FEM formulations of ERMES and CST are available in reference [15], shedding light on the superior performance of ERMES in certain applications. The introduction within the section elaborates on the rationale behind choosing FEM FD for the NEXTGEM project, emphasizing its suitability. A key advantage setting ERMES apart from its commercial counterparts is its open-source nature. Offering transparency into the methodology for each case, ERMES invites users to explore every facet of the algorithm and data. This accessibility fosters adaptability, enabling users to expand the code according to their specific modelling requirements. Notably, ERMES stands as a free and open-source solution, breaking barriers and empowering the broader scientific community.

ERMES is available for Windows and Linux operative systems and has a user-friendly interface integrated in the pre- and post- processor GiD [22]. GiD is used for geometrical modelling, data input, meshing and visualization of results. GiD allows us to define material properties, apply boundary conditions and work with complex geometries in various CAD formats. It also makes the visualization of results simple and effective.

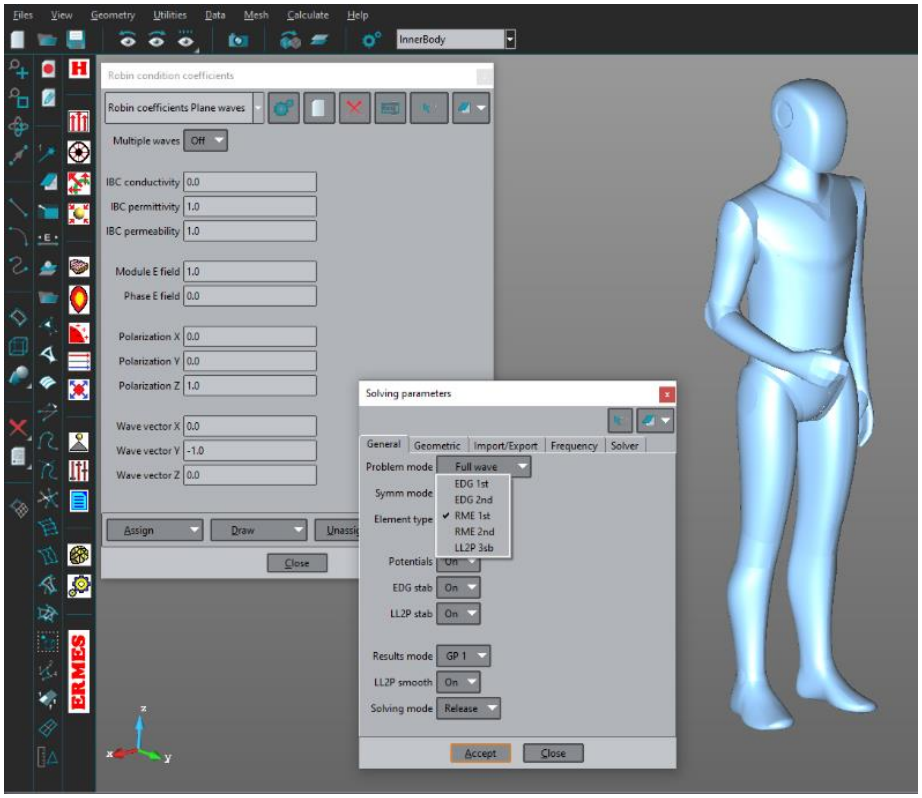

Figure 15: ERMES graphical user interface integrated in the pre- and post- processor GiD [22]

ERMES is under the open-source software 2-Clause BSD License [23] and it can be downloaded for free from the Computer Physics Communications Program Library [13] or from the software section of the developer website [24]. The version presently available for download is the old version ERMESv7.0. The release of the new version ERMESv20.0 is planned to be before the end of 2023. ERMESv20.0 will include all the new features mentioned

in this report and it will be available to download from the mentioned websites (Otin, ERMES: A nodal-based finite element code for electromagnetic simulations in frequency domain, 2013; Otin, ERMES - Software, n.d.).

4.2 New ERMES features for NextGEM

ERMES has been customized to make the simulation of the scenarios described in Section 2 possible. More features could be added in the future if it is required for any particular scenario. Up to this date, the new features added to ERMES for NextGEM are:

- Plane waves excitation (single and multiple waves, see Figure 16).
- Gaussian beam excitation.
- Discontinuity surfaces (better internal/external field visualization, see Figure 17).
- Stabilized edge 1st and 2nd order FEM formulation.
- Local L2 projection FEM formulation.
- Extended Impedance Boundary Conditions [25][26] (see Figure 18).
- PETSc [27] interface with ERMES (improved HPC capabilities).

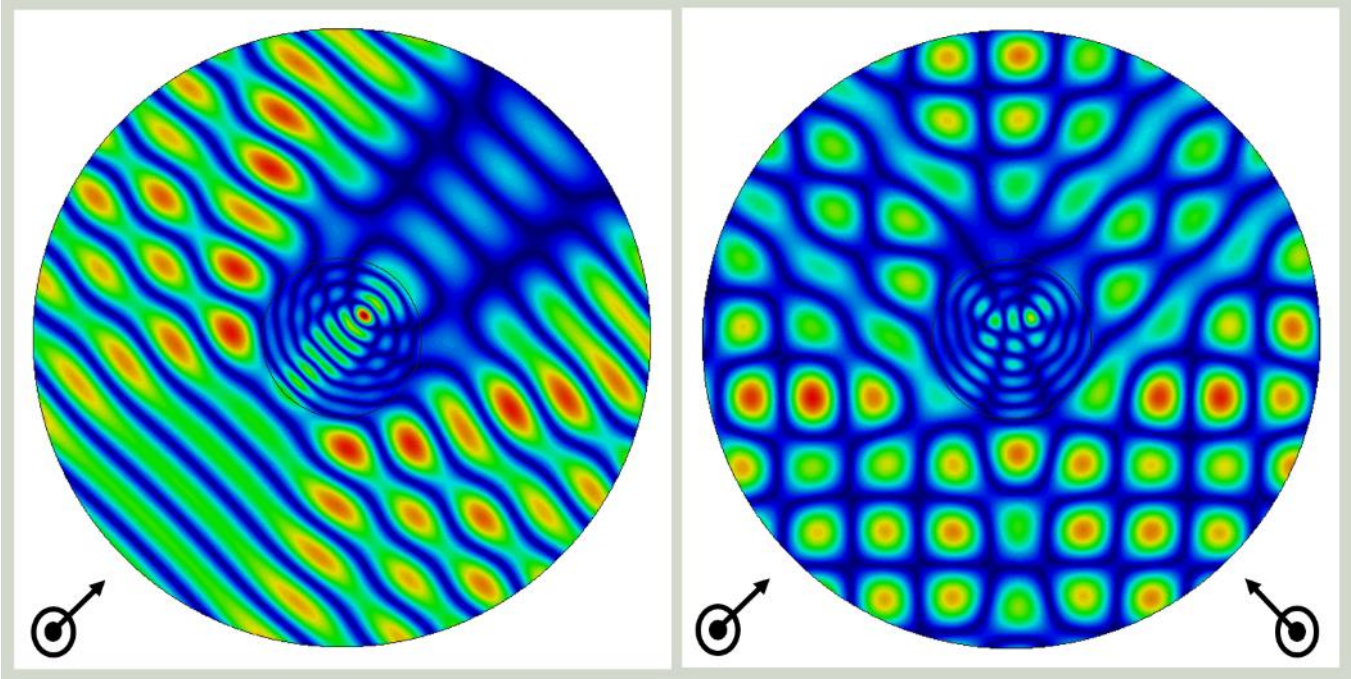

Figure 16: Electric field module of a single (left) and multiple (right) plane wave illumination of a dielectric cylinder.

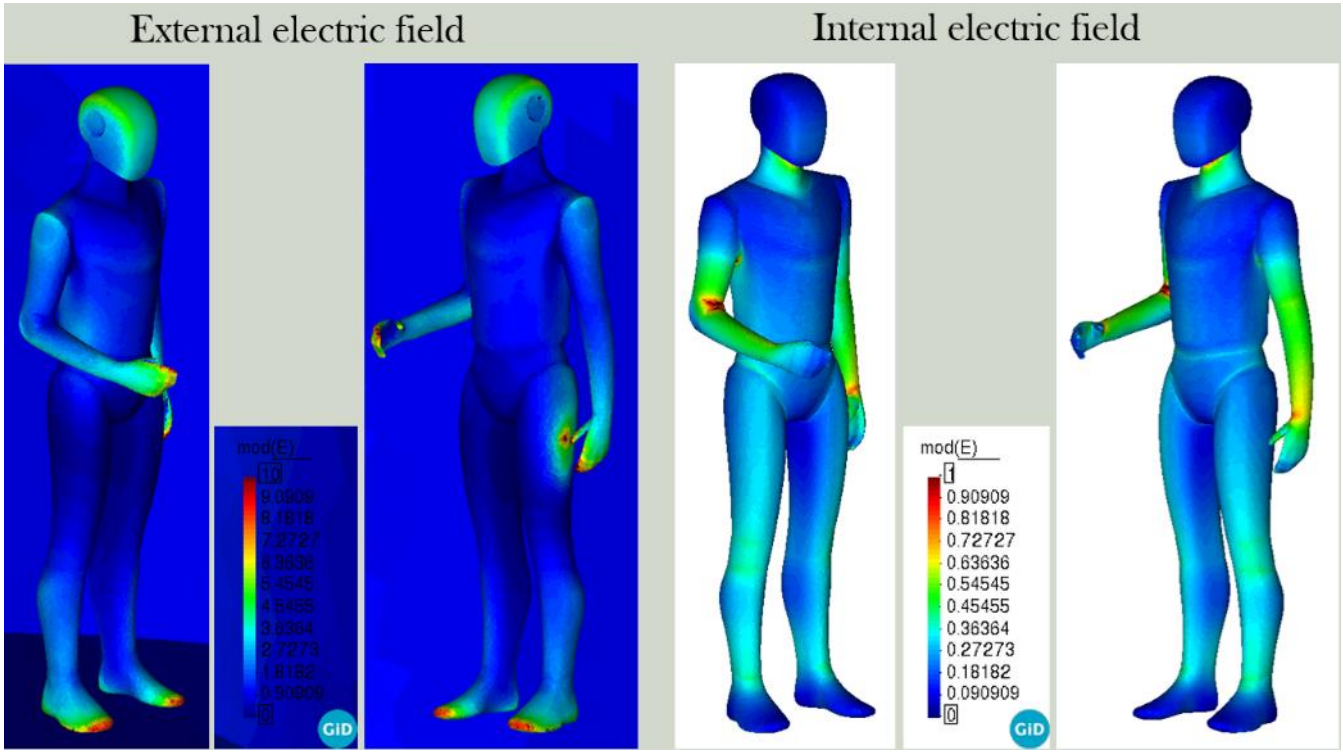

Figure 17: Dummy irradiated by a frontal plane wave. External (left) and internal (right) electric field.

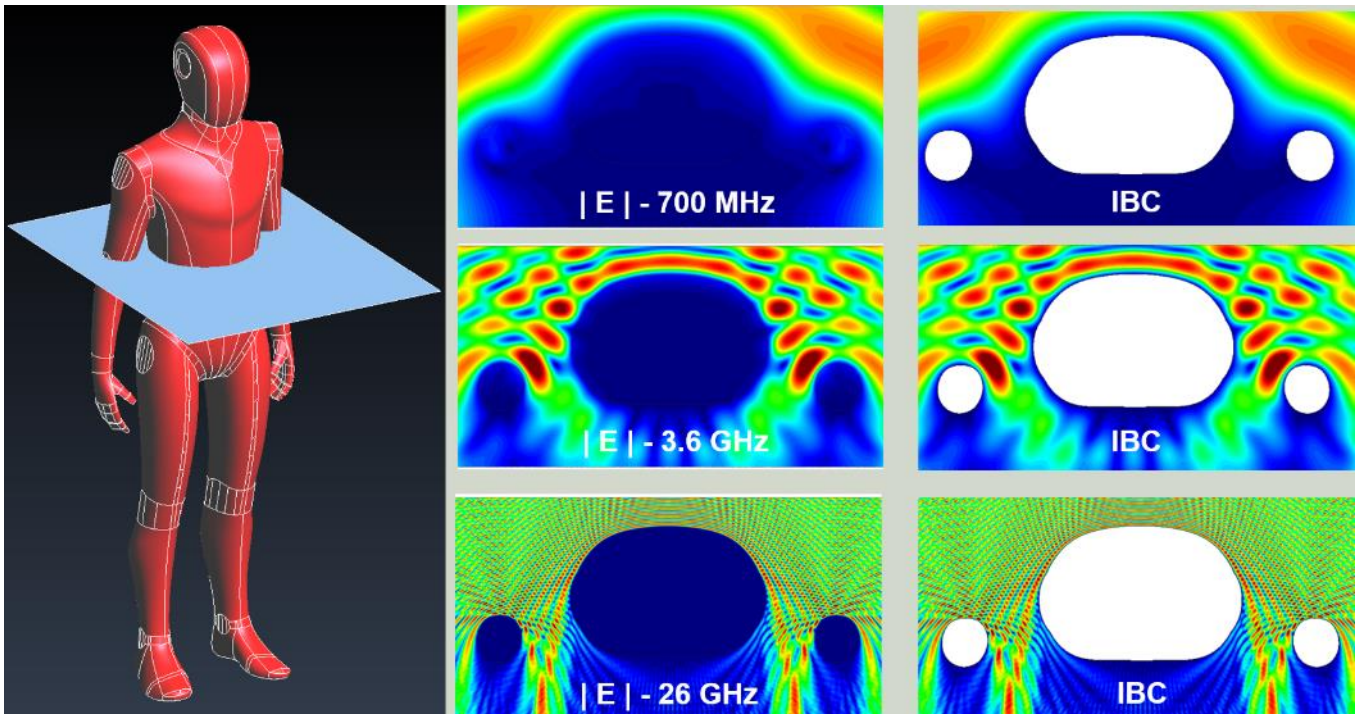

Figure 18: Example of application of the Impedance Boundary Conditions (IBC) [25][26] on the surface of a dummy irradiated with a frontal plane wave at three different frequencies (visualization of the cross-section fields on the right). IBC provides the same external fields that a full volumetric model at higher frequencies (when the fields do not penetrate much into the body) avoiding the volumetric mesh inside the dummy and saving computational resources.

4.3 Embedding of ERMES WS in NextGEM

The aim of incorporating ERMES into the NIKH platform for numerical simulation holds significant importance in the framework of the NextGEM project. ERMES, as open-source software, brings a range of advantages that enhance accessibility, collaboration, transparency, and innovation in the realm of numerical simulations. In the specific context of electromagnetic fields associated with 5G and 6G technologies, where there are perceived

concerns and challenges from society, the adoption of open-source codes, like ERMES, serves as a powerful tool to dispel doubts and promote a deeper understanding of real impacts.

The availability of open-source tools fosters inclusivity and widespread access. Users can leverage the use of ERMES without the barriers of licensing costs, making advanced simulation capabilities accessible to a broader audience, including researchers, students, professionals, and the general public. This translates into a substantial increase in the credibility of results and the ability to replicate and validate experiments, which is essential in the context of scientific research.

Collaboration is another key aspect of the NextGEM project. By embedding ERMES into the NIKH platform, developers and researchers can harness the collective intelligence of the global community. This collaborative model enables continuous improvement and the development of new features, benefiting from the diverse expertise of contributors worldwide. This collaborative ecosystem provides valuable resources for individuals looking to learn and apply numerical simulation techniques. It also facilitates the exchange of ideas, fostering a supportive environment for continuous learning and skill development. The transparency of ERMES promotes trust, allowing users to inspect, modify, and customize the software to suit their specific needs.

Moreover, the adaptability of ERMES contributes to innovation in numerical simulations. Users can extend the functionality of the tools, implement custom algorithms, and tailor the software to address specific challenges in various domains. This flexibility empowers researchers and engineers to explore novel approaches, accelerating the pace of discovery and problem-solving. The incorporation of ERMES into the NIKH platform also aligns with the principles of reproducibility and transparency in scientific research in the European framework. Users can inspect and validate the algorithms and methodologies employed in simulations, ensuring the reliability of results. This transparency is crucial for building trust in computational electromagnetics findings and fostering a culture of open scientific inquiry.

In conclusion, embedding ERMES into the NIKH platform for numerical simulation promotes accessibility, collaboration, innovation, transparency, and reproducibility. This transparency strengthens the credibility of studies and contributes to building consensus based on evidence. This initiative not only addresses the concerns of the most sceptical but also promotes a transparent and collaborative approach to advanced electromagnetic phenomena research.

5 Numerical models for NextGEM

We will follow different modelling strategies depending on the scenario under consideration. The main differences between the strategies rest in the relative electric size of the problem domain (λ/D) and the location of the EMF sources. For electrically large problems, we will use a high-frequency method coupled with FEM. The FEM volumetric domain will be illuminated through a boundary condition representing the EMF intensity calculated with the high-frequency method on that location. If the frequency is high enough, we will use the IBC approximation shown in Figure 18 instead of a volumetric model of the body. On the other hand, if the EMF source is close enough, it will be included in the problem domain and solved on the same FEM volume as the irradiated sample. The IBC approximation could also be used in this case if there is low penetration of the fields inside the body.

In this section we are going to show some preliminary EMF modelling performed since the start of NextGEM until the delivery of this report (November 2023). The next deliverable D3.6 will show the results of the simulations for all the scenarios presented in Section 2.

5.1 Examples in the FR1 range

The first example corresponds to the scenario described in Section 2.1. A far EMF source irradiates a homogenous dummy at frequencies 0.7 GHz, 1.9 GHz, and 3.0 GHz. The EMF source is placed in a complex environment that causes multiple reflections and illuminates the dummy with different angles and polarizations. The objective of these simulations is to obtain the optimal location for the electric field measurement devices that are going to be installed in a vest that some volunteers are going to wear while walking in the complex environment. Also, we want to correlate the external electric field measured in the vest detectors with the field inside the dummy.

5.1.1 Dummy model in the FR1 range

For the 0.7 GHz case we used a volumetric dummy that was irradiated with plane waves of 1 V/m of amplitude and different polarizations and wave vector directions. The fields were averaged afterwards to obtain the best locations of the detectors. In Figure 19 we can see the electric field produced by a frontal plane wave vertically polarized. In Figure 19 is also shown a frontal wave but horizontally polarized. It is clearly observable how the polarization of the wave affects the field distribution on the external surface of the dummy.

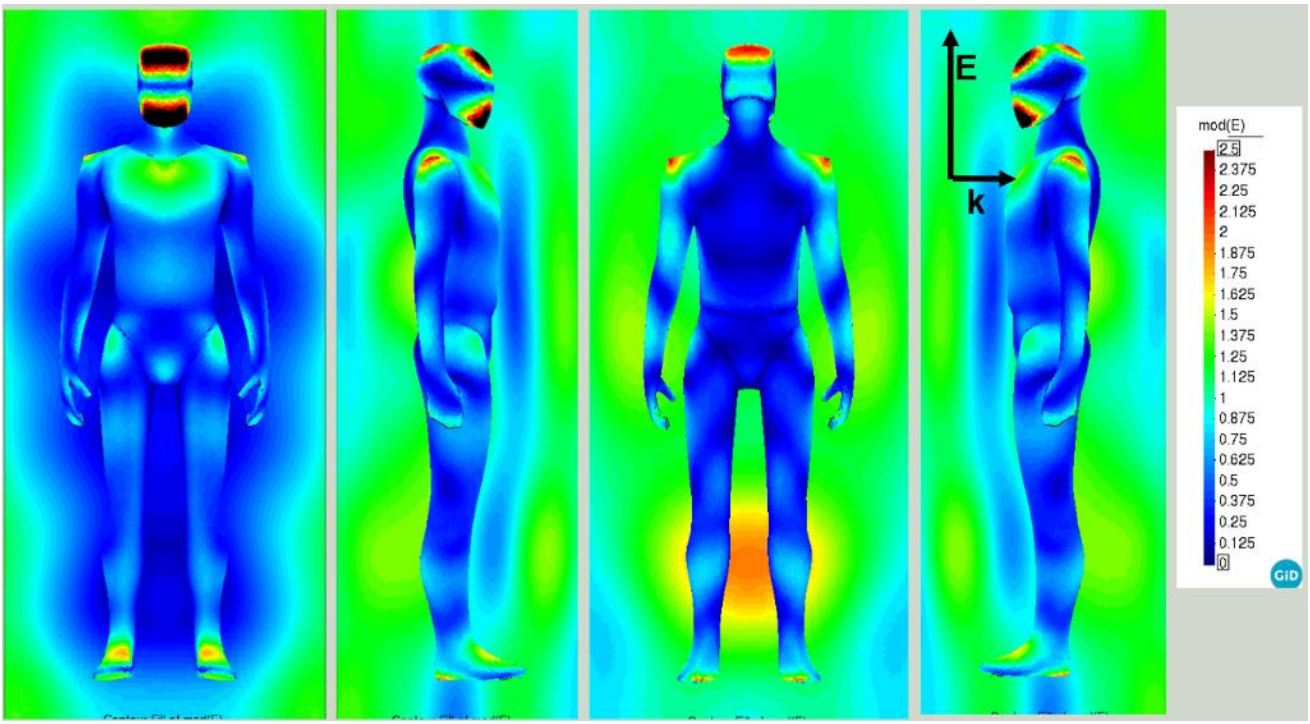

Figure 19: External electric field generated by a frontal wave vertically polarized at 0.7 GHz.

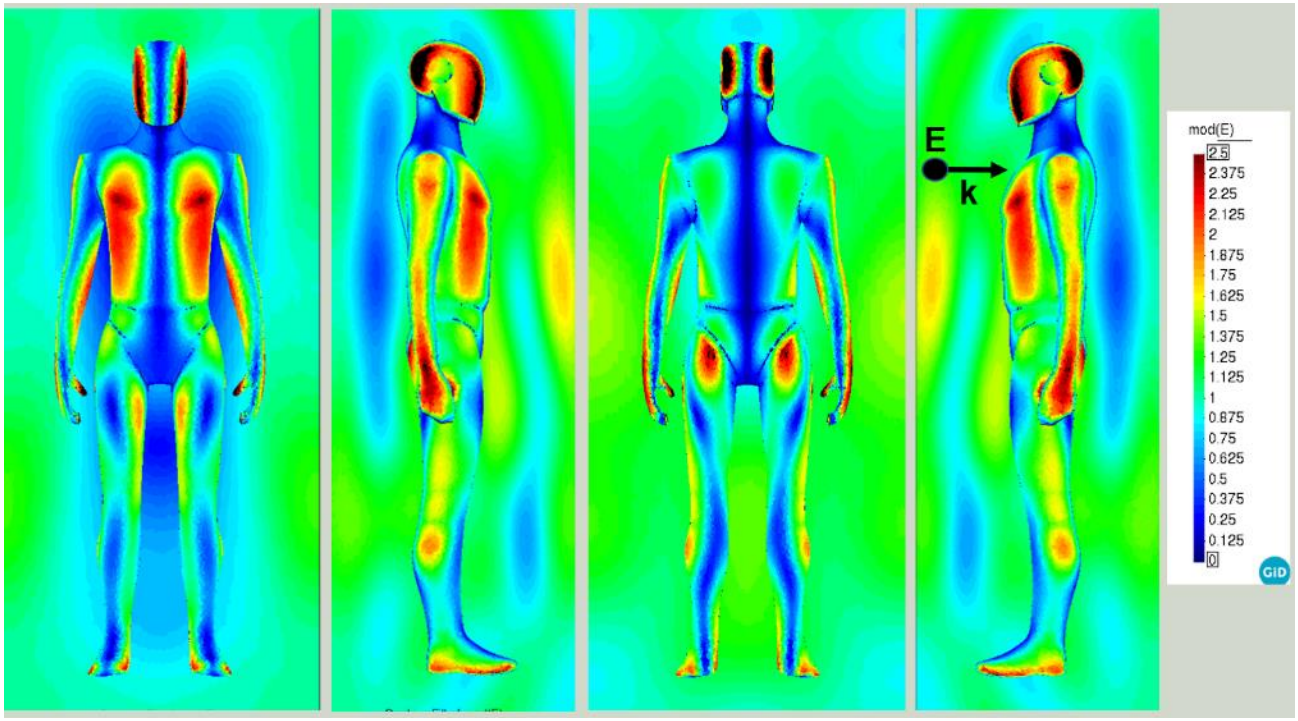

Figure 20: External electric field generated by a frontal wave horizontally polarized at 0.7 GHz.

The average over all the polarizations and directions is shown in Figure 20. The average is made over five different wave directions (frontal, back, left, right and top) with two polarizations each (horizontal and vertical) adding a total of ten independent simulations. Figure 21 shows that the best locations for the detectors are in the head, shoulders, arms, and chest of the dummy.

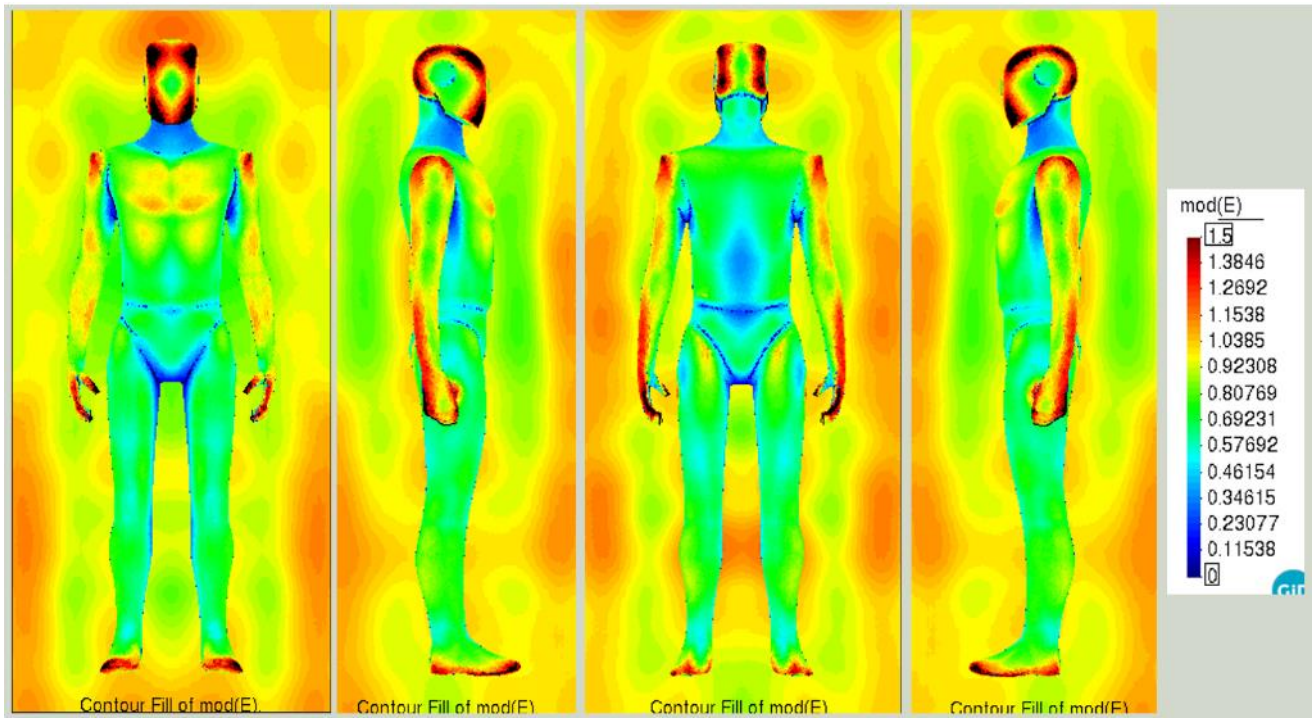

Figure 21: Average external electric field over five different wave directions (frontal, back, left, right and top) with two polarizations each (horizontal and vertical) adding a total of ten independent simulations.

The internal electric fields were obtained for the same cases as for the external fields shown above. In Figure 22 and Figure 23, we can see the internal electric field for the vertical and horizontal polarization cases, respectively. We can appreciate in these figures the differences between the internal and external electric field distribution shown

in Figure 20 and Figure 21. The differences are caused by the discontinuity of the fields on the materials' interfaces. Figure 24 shows the average of the internal fields following a similar procedure as the one explained in Figure 21.

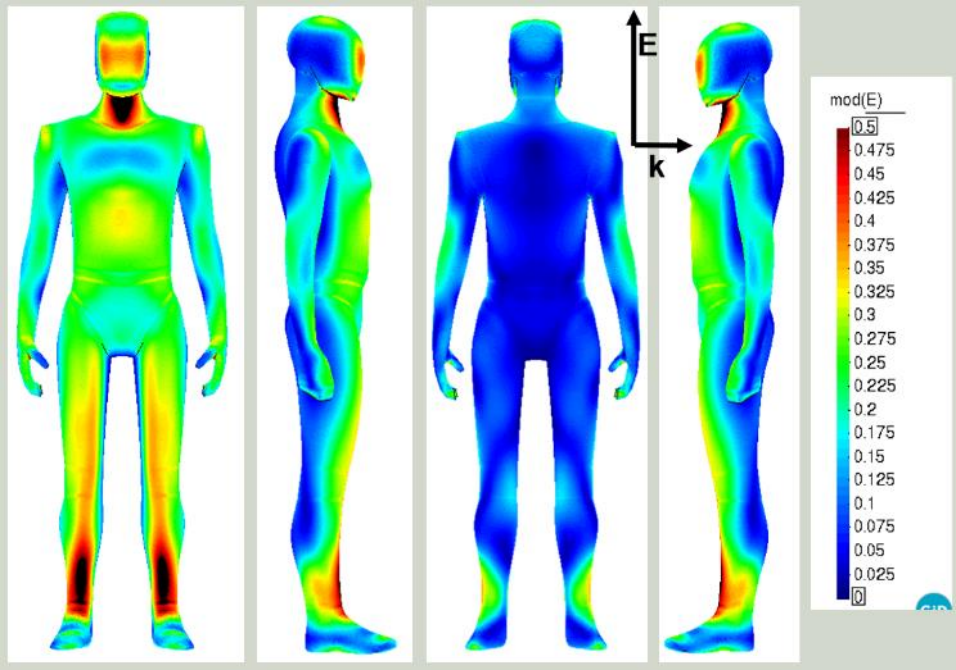

Figure 22: Internal electric field generated by a frontal wave vertically polarized at 0.7 GHz.

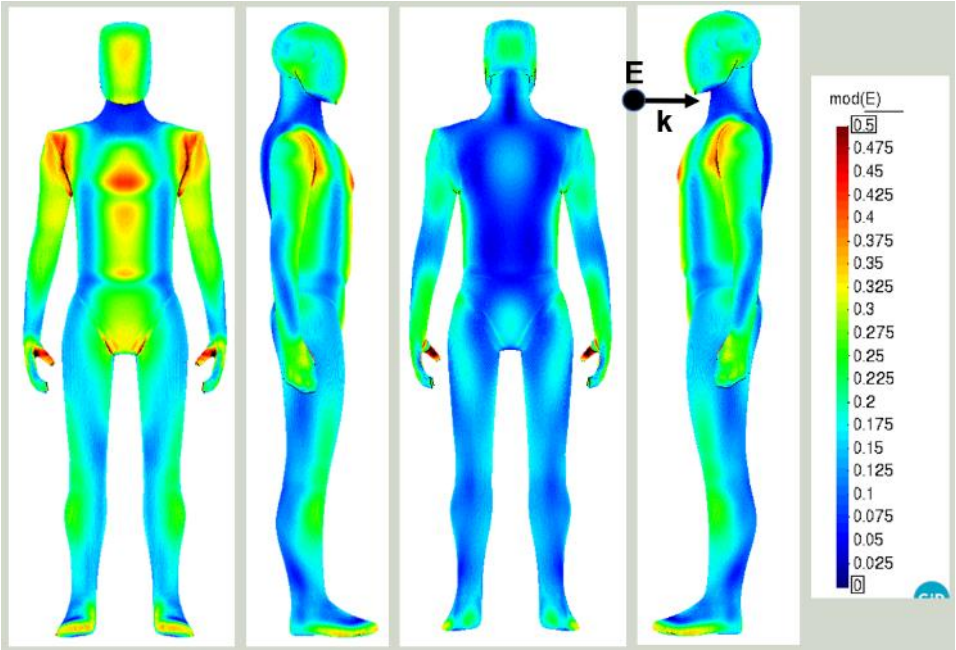

Figure 23: Internal electric field generated by a frontal wave horizontally polarized at 0.7 GHz.

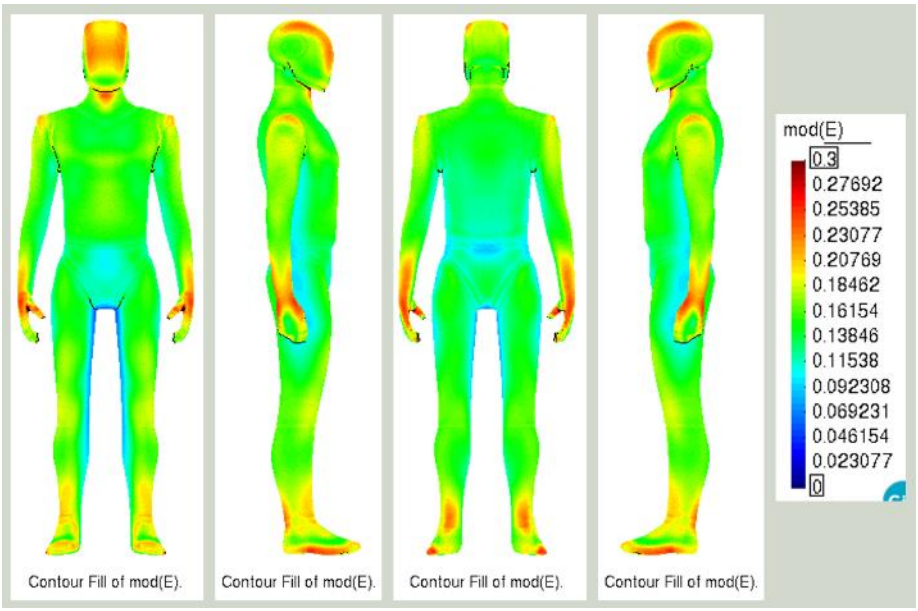

Figure 24: Average internal electric field over five different wave directions (frontal, back, left, right and top) with two polarizations each (horizontal and vertical) adding a total of ten independent simulations.

For the frequencies 1.9 GHz and 3.0 GHz, we follow a similar strategy as the one explained above, but this time, we used the IBC approximation on the dummy surface to save computational resources. In Figure 25, it is shown the external electric field for a vertically polarized frontal plane wave is shown (as in Figure 19). We can appreciate the differences in the field distributions for the different frequencies. Also, we can observe a slight difference in the 0.7 GHz case when compared with the previously calculated. This is because for the 0.7 GHz case, the IBC model is not as good approximation as for the higher frequencies due to the deeper penetration of the fields inside the body (see Figure 23).

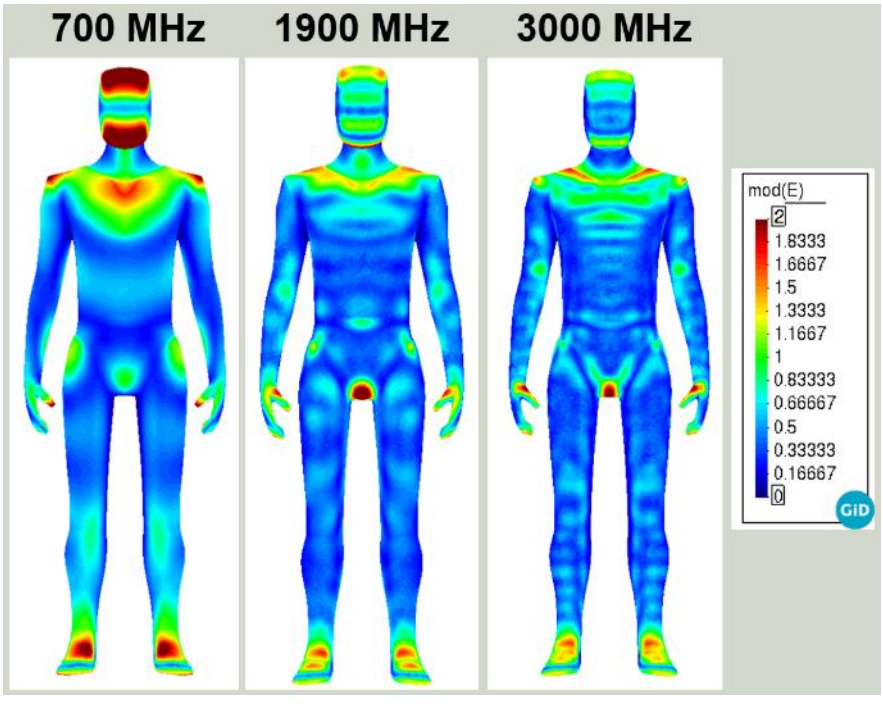

Figure 25: External electric field generated by a frontal wave vertically polarized at 0.7, 1.9 and 3.0 GHz. IBC model approximation.

In the IBC approximation, we use the magnetic field on the surface of the dummy to calculate the power absorbed inside the dummy. The power absorbed per unit surface inside the dummy can be expressed as (Pozar, 1998):

$P_S = \frac{1}{2}\boldsymbol{R_S}|\boldsymbol{H_t}|^2$ where $\boldsymbol{R_S}$ is the surface resistance (which depends on the material properties of the first layers of the dummy), and $\boldsymbol{H_t}$ is the component of the magnetic field tangential to the IBC surface. Figure 26 shows the

magnetic field distribution on the surface of the dummy for the three frequencies for the frontal wave vertically polarized case.

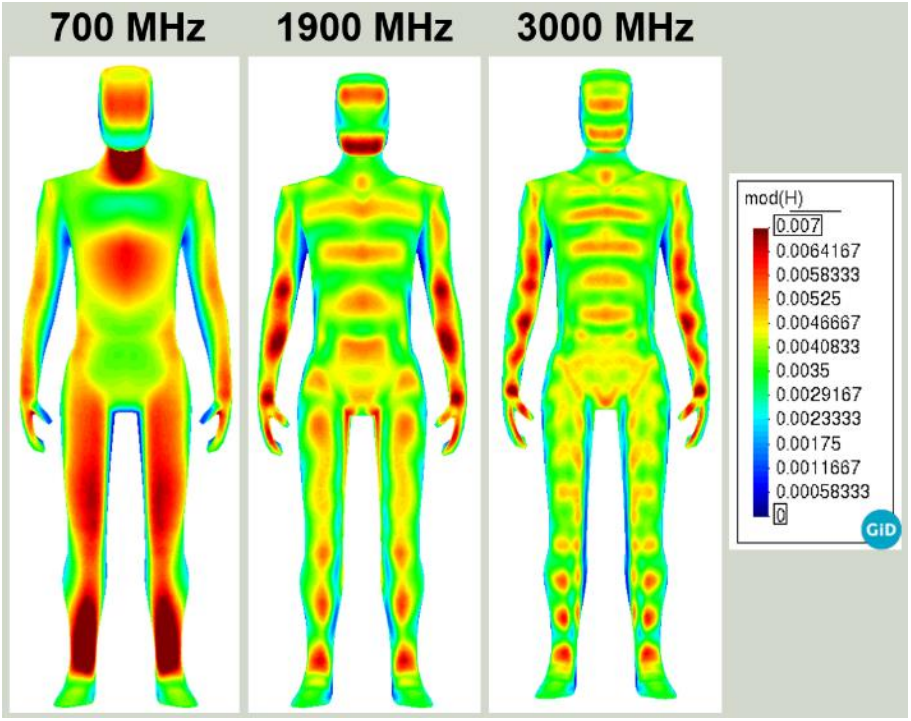

Figure 26: Magnetic field distribution generated by a frontal wave vertically polarized at 0.7, 1.9 and 3.0 GHz. For the IBC model approximation, the power absorbed by the dummy can be calculated from the magnetic field H on the surface [28]

5.1.2 Skin model in the FR1 range

5.1.2.1 Skin model

In this section, the human skin model defined in Section 3.2 was modified, with the objective of analyzing the effects of the electromagnetic field on the blood. For this, a small arteriole (0.2mm) was created in the dermis layer (see Figure 27), and a vacuum layer was added on the top of the stratum corneum. Note, that the surface area of the skin model is a square with dimensions of 0.4 mm x 0.4 mm, and it extends to a depth of 1.5 mm. In Figure 27, the different layers of the model are represented:

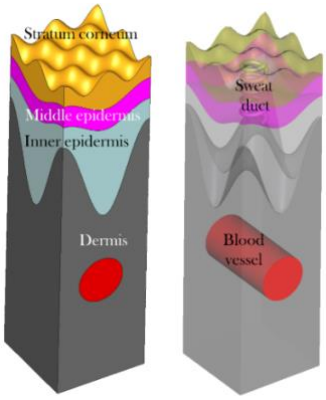

Figure 27: Modified skin model

The electromagnetic properties of different layers of human skin (dry) at 700 MHz and 3,5 GHz are a critical component of this modelling effort. To do that, we used the following equations:

$$\varepsilon_c = \epsilon_c + i\frac{\sigma_c}{\omega} = \epsilon' - \frac{\sigma''}{\omega} + i\left(\epsilon'' + \frac{\sigma'}{\omega}\right) \quad \text{Eq.1}$$

$$\sigma_c = \sigma' + i\sigma'' \quad \text{Eq.2}$$

$$\epsilon_c = \epsilon' + i\epsilon'' \quad \text{Eq.3}$$

These equations correspond to the total complex permittivity ($\boldsymbol{\epsilon_c}$) and complex conductivity ($\boldsymbol{\sigma_c}$). In $\boldsymbol{\epsilon_c}$ [Eq.3], $\boldsymbol{\epsilon'}$ is the real part of permittivity, which is associated with the material's ability to store electric energy, and $\boldsymbol{\epsilon''}$ is the imaginary part of permittivity, which is related to energy dissipation due to bonded charges. In $\boldsymbol{\sigma_c}$ [Eq. 2], $\boldsymbol{\sigma'}$ is the real part of conductivity, related to the material's direct conductivity and energy dissipation due to free charges, and $\boldsymbol{\sigma''}$ is the imaginary part of conductivity, associated with the ability of the material to store electromagnetic energy ($\boldsymbol{\sigma''}$ can be neglected at the frequencies of interest of this report, so $\boldsymbol{\sigma''} = 0$ in the following). For the material losses, we have considered an equivalent conductivity which encompasses all the losses $\boldsymbol{\sigma_e = w\epsilon'' + \sigma'}$. This is done because from the experimental point of view, the origins of the losses are indistinguishable, and the only results obtained from the experiments are the real and imaginary parts of the total permittivity $\boldsymbol{\varepsilon_c}$. So, in Eq. 1 we will consider $\boldsymbol{\sigma'' = 0, \epsilon'' = 0}$ and $\boldsymbol{\epsilon', \sigma_e = \sigma'}$ will be taken from the material properties tables.

Table 3 shows the relative real permittivity and real conductivity used for characterizing the different layers of the skin model for 700 MHz and 3.5 GHz.

Table 3: Electromagnetic properties of the human skin for 700MHz and 3.5GHz

700 MHz		
Layer	ε' / ε₀	σ' (S/m)
Stratum Corneum	42.70	0.80
Sweat duct	77.00	2.00
Middle epidermis	39.50	0.45
Inner epidermis	39.50	0.45
Dermis	41.27	0.65
Blood vessel	62.54	1.36

3.5 GHz		
Layer	ε' / ε₀	σ' (S/m)
Stratum Corneum	37.00	2.02
Sweat duct	75.00	4.00
Middle epidermis	34.55	1.70
Inner epidermis	34.55	1.70
Dermis	38.43	2.49
Blood vessel	64.03	3.83

The dielectric properties used in this study were sourced from the Tissue Dielectric Properties for Electromagnetic Modelling of the Human Body database [29]. The data for the dermis and epidermis are of particular significance, having been derived from Sasaki, K. et al. [31] at the National Institute of Information and Communications Technology in Tokyo, based on experiments involving pig models. Most prior studies were conducted in vitro using non-destructive probes. However, the measurements from Sasaki's work reflect the physiological state of tissues in vivo, accounting for factors such as basal metabolism and blood flow, which are often neglected during in vitro studies involving excised tissues [29][31]. These data were cross-referenced for validation with dielectric property measurements from the Nello Carrara Center for Applied Physics in Florence, Italy [30]. The magnitude of the values showed strong agreement between the two sources. In the case of blood properties, the values from both studies were averaged to ensure a more comprehensive representation. The epidermis was modelled by assigning identical properties to the "Middle Epidermis" and "Inner Epidermis" layers due to the granularity of the model's subdivision. For the Stratum Corneum (the outermost layer of the skin), the "Skin Dry" properties from IFAC (Nello Carrara Center) were used, simulating a non-sweating condition [30]

Table 4: Properties of the artificial sweat solution under test [33]

Base component	Concentration of components (g/L)				
	Over-Concentrated (4%)	Concentrated (2%)	Standard (1%)	Diluted (0.5%)	Over-diluted (0.25%)
NaCl	20 g	10 g	5 g	2.5 g	1.25 g
KCl	4 g	2 g	1 g	0.5 g	0.25 g
Urea	4 g	2 g	1 g	0.5 g	0.25 g
Lactic acid	4 g	2 g	1 g	0.5 g	0.25 g

Regarding the sweat duct, its dielectric properties are reasonably approximated by those of water. However, the actual properties are influenced by the concentration of minerals, urea, and alcohol present in sweat, as well as the subject's hydration level. A study from the United Kingdom further investigated sweat properties using a saline solution designed to mimic human sweat closely. This artificial sweat was synthesized in accordance with the European standard EN1811:2011. The solution formulation involved dissolving 0.5% NaCl, 0.1% KCl, 0.1% lactic acid, and 0.1% urea in 1 liter of distilled water. Five distinct solutions with varying concentrations of metabolites and minerals were prepared, as depicted in Table 4. These solutions spanned a range of sweat compositions typically observed under different hydration conditions. All measurements were carried out at a controlled room temperature of 23°C [20].

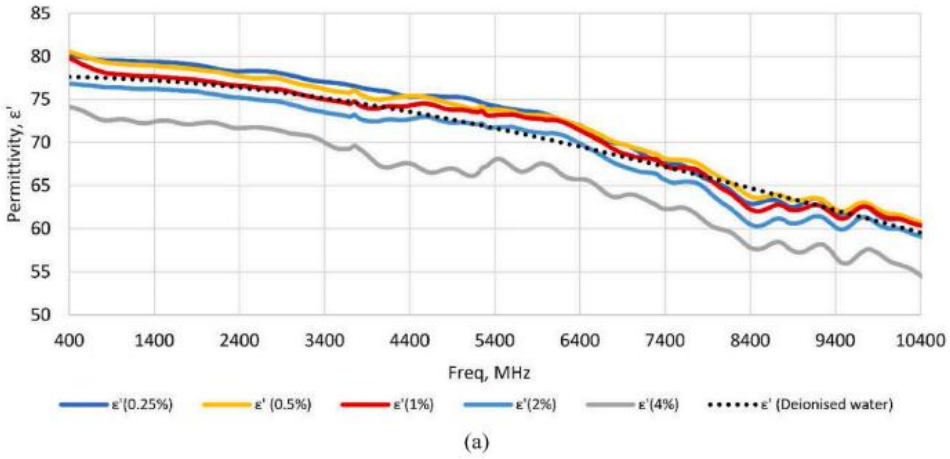

Figure 28: Sweat Permittivity (23°C) at different frequencies [33]

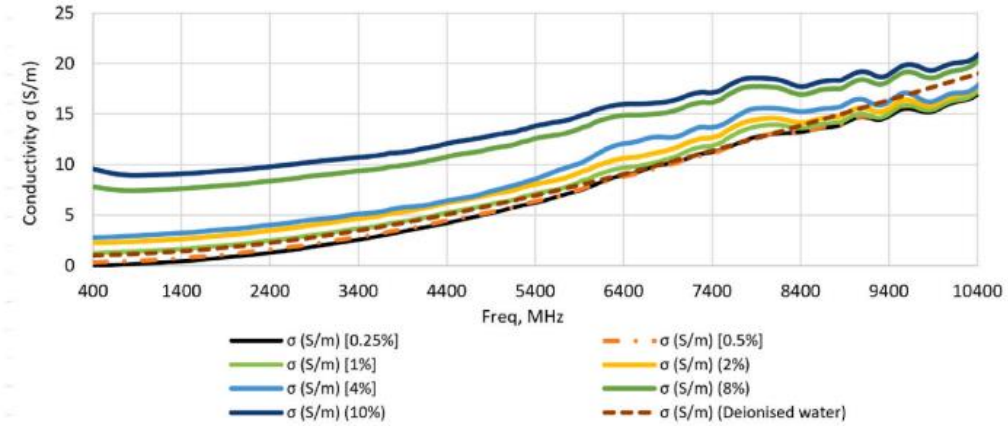

Figure 29: Sweat Conductivity (23°C) at different frequencies [33]

Additionally, a study conducted by the Department of Chemistry at Rice University was reviewed, in which a similar experiment was performed at 25°C using a saline solution closely resembling that from the UK study [34]. The resulting graph, shown in Figure 30, indicates that the dielectric properties at 700 MHz and 3 GHz were highly consistent between the two studies.

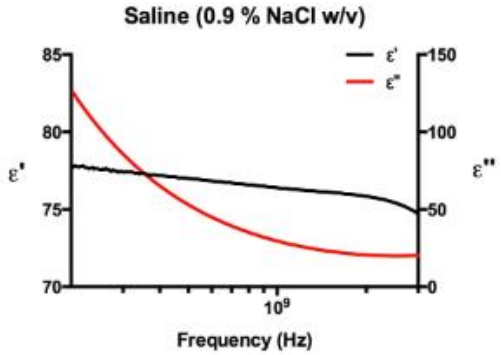

Figure 30: Permittivity of a saline water (very similar to the sweat) [34]

The left side of the graph illustrates the real part of the permittivity, while the right side shows the imaginary part. At 700 MHz, the real permittivity was around 77, with an imaginary component of 40 F/m, and a conductivity of 2 S/m, consistent with both studies. At 3.5 GHz, the real and imaginary permittivity values were 75 and 20 F/m, respectively, with a conductivity of 4 S/m. For the higher frequency range of 26 GHz, reference was made to a separate study conducted by Eldamak et al. at the Faculty of Engineering, Cairo University [35].

To quantify the energy absorbed by the blood within the arteriole from the electromagnetic field, the Specific Absorption Rate (SAR) was computed for the exposed region. SAR calculation is based on the tissue's electromagnetic properties and the magnitude of the electric field. After characterizing the electromagnetic

properties of human skin, the skin model was irradiated with plane waves of 1 V/m of amplitude and "y" polarization. Figure 31 shows the distribution of the electric field and joule heating across each layer of the skin model produced by a frontal plane wave horizontally polarized. Importantly, SAR values were specifically computed for the arteriole (blood vessel). The results show that SAR values in the arteriole reach 0.04 mW/kg at 700 MHz and 0.12 mW/kg at 3.5 GHz. This variation in SAR can be explained by the frequency-dependent nature of tissue interaction with electromagnetic fields. The fields reaching the arteriole have similar values at both frequencies, but at 700 MHz the equivalent conductivity is several times lower than at 3.5 GHz, which leads to a reduced absorption of energy. Simulations were performed with ERMES (version 20).

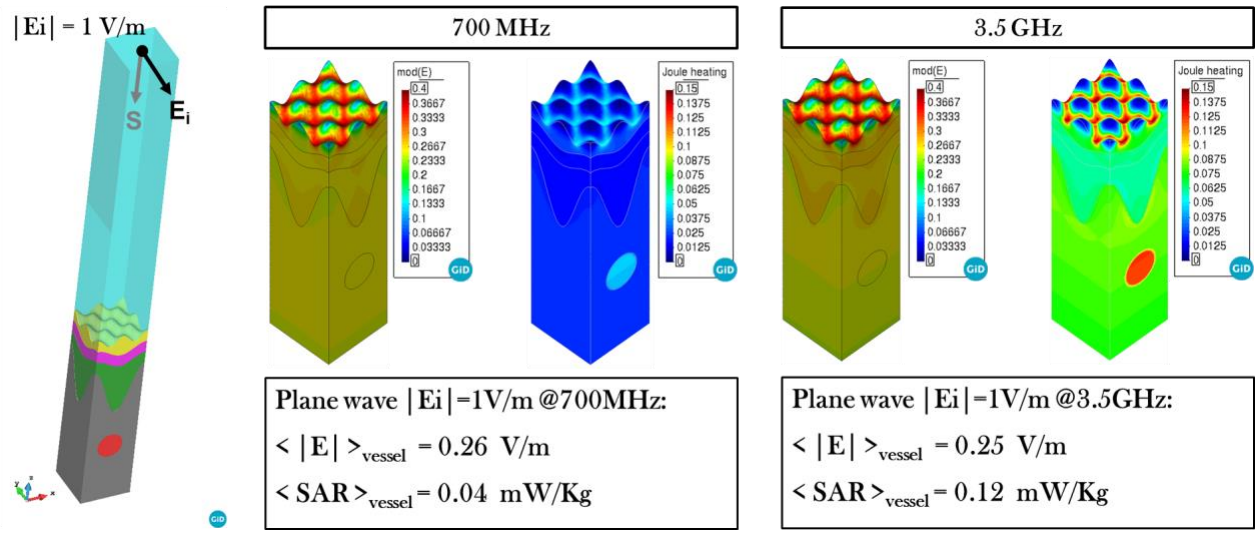

Figure 31: Numerical simulation of the skin model at 700 MHz and 3.5 GHz

It is important to note that the SAR values obtained were calculated based on an incident electric field of 1 V/m, as a reference. However, typical outdoor exposure scenarios, especially at FR1 frequencies, may involve lower field strengths. To reflect more realistic conditions, the SAR values can be scaled accordingly. For example, if the incident field strength in a typical outdoor environment is lower, such as 0.6 V/m, the SAR values would decrease proportionally, resulting in scaled SAR values of approximately 0.0144 mW/kg at 700 MHz and 0.0432 mW/kg at 3.5 GHz. This adjustment provides a more accurate estimation of energy absorption for real-world exposure conditions.

5.2 Challenges and adopted approaches for the FR2 range

In Chapter 2, the various meshing strategies for full body and surface models have been introduced. At this stage it is important to remind the reader that the number of cells used will depend on the shape of the object in the model as well as on the operation frequency at which the simulation is performed. A sufficient number of meshing cells (i.e., the defined cells where the governing equations of the simulator will be solved, in an EM solver those are Maxwell's equation and the boundaries conditions) is required to extract the accurate electromagnetic response of the object under simulation. In practical conditions, this could be done in the order of 10 cells per wavelength. To give an implication of the impact of computation time of this statement when attempting to perform simulation in the FR2 band, let us consider the following example of *meshing of HUGO head with mobile phone*.

Considering a model with voxels of 1mm x 1mm x 1mm, where the background was meshed with 10 cells per wavelength, but two different mesh cells were used for local mesh: 0.25 mm and 0.21 mm. This was done in order to have some discretization in the voxels and in the mobile phone components with dimensions of the order of millimetres. When attempting to perform this simulation at 1800 MHz, with a local mesh of 0.25mm, the smallest cell was 0.23mm, and the overall number of cells was about 107 million. With a local mesh of 0.21, the smallest cell was 0.19mm, and the overall number of cells was about 200 million.

When running this simulation on an AMD Ryzen 9 5950X, 16 cores operating at 3.4 GHz, 128GB RAM with an NVIDIA GeForce RTX 3090, the two simulations took 6h40' and 23h, respectively. This also shows given the matrix and floating-point operations, that the time is not linear to the number of cells.

If we were to attempt to run a similar simulation at 26 GHz, the (free space) wavelength would be about 11mm, so that the background meshcell would scale to about 1mm. Consequently, the local mesh would still be finer than the background mesh, given the higher medium permittivity of the medium in the head a scaling factor would

(probably) still be needed for the local mesh, which would lead to impractical computation times for the analysis to be performed in the project.

For the above reasons within the NextGEM project the approach to access, install and operate ERMES on different high-performance supercomputer installations were implemented in the first part of the project. To quantify the expected computational resource improvement, we need to consider state of the art server level (i.e., single high-power computer) performance. These are reported for one specific vendor in Figure 27.

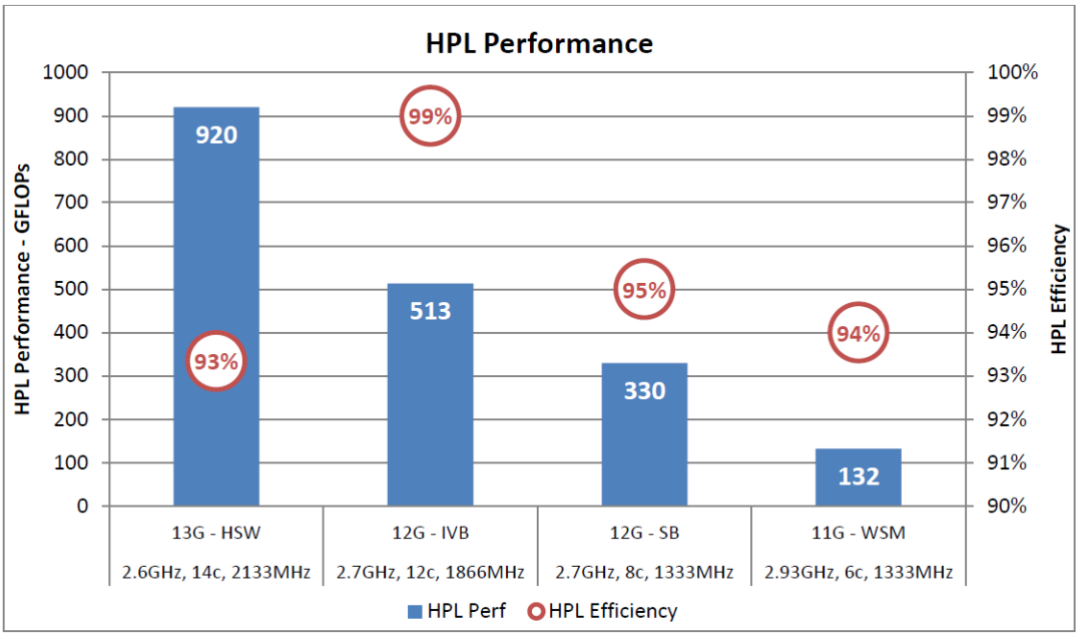

Figure 32: HPL Performance (DelfBlue)

The reported value shows the capability of close to 1 tera Flop per second (i.e., 1e12 floating point operations per second). To report the computational improvement that can be expected using a supercomputer cluster we report here the number of one of the systems that is being setup by the NextGEM consortium to run simulations, other systems are also being installed.

The numbers here are based on the Delft Blue supercomputer [3].

The cluster consists of three different types of compute nodes:

- Standard compute nodes
- Fat compute nodes (large memory) in 2 memory configurations
- Compute nodes with CPU's equipped with NVIDIA Tesla cards

Table 5: Delft Blue Node types.

Node Category	Number	Cores	CPU / GPU	Memory	SSD
Standard	218	48	2x Intel XEON E5-6248R 24C 3.0GHz	192 GB	480 GB
Fat type-a	6	48	2x Intel XEON E5-6248R 24C 3.0GHz	768 GB	480 GB
Fat type-b	4	48	2x Intel XEON E5-6248R 24C 3.0GHz	1536 GB	480 GB
GPU	10	48	2x AMD EPYC 7402 24C 2.80 GHz 4x NVIDIA Tesla V100S 32GB	256 GB	

[3] https://www.tudelft.nl/dhpc/system

Table 6: Summary of the system and performance.

CPU total	Compute nodes	238
	CPU's	476
	Compute cores	11424
	Rpeak (theoretical max. performance, in PFlops)	1.05
GPU total	GPU nodes	10
	GPU's	40
	Tensor cores	25600
	CUDA cores	204800
	Double Precision (theoretical max. performance, in TFlops)	328
	Single Precision (theoretical max. performance, in TFlops)	656
	Deep Learning (theoretical max. performance, in PFlops)	5.2

The high-performance computer cluster provides as peak value ~1 Peta flops. This results in 3 orders of magnitude higher floating-point operations per second, considerably expanding the computational capability to address the FR2 cases.

5.2.1 Skin model in the FR2 range

For the FR2 range, we use the modified skin human model described in Section 5.1.2.1. To characterize the electromagnetic properties for the different layer we used the previous studies [29][30][31]. Table 7 shows the electromagnetic properties used for this study.

Table 7: Electromagnetic properties at 26GHz.

Layer	$\varepsilon' / \varepsilon_0$	σ' (S/m)
Stratum Corneum	17.41	24.78
Sweat duct	23.20	0.01
Middle epidermis	16.95	19.61
Inner epidermis	16.95	19.61
Dermis	14.95	21.41
Blood vessel	25.03	41.27

However, for the duct system, we used the study conducted by Eldamak et al. [35]. In the Eldamak et al study the dielectric measurements were performed on aqueous solutions of sodium chloride (NaCl), potassium chloride (KCl), urea, and lactic acid, along with their various mixtures. These combinations were designed to simulate artificial sweat under different hydration levels. The complex dielectric permittivity of all solutions and mixtures was analyzed over a frequency range of 1-20 GHz at a temperature of 23°C, with ionic concentrations varying between 0.01 and 1.7 mol/L. The formulation of the artificial sweat followed the European standard EN1811:2011, which specifies a recipe of 0.5% NaCl, 0.1% urea, and 0.1% lactic acid dissolved in 1 litre of distilled water, although this was slightly modified in the study [27].

For our analysis, we selected a salt concentration that reflects a subject with normal hydration, consistent with the methodology used in previous cases. Section 3.3of the Eldamak et al. paper presents the experimental results for the artificial sweat mixtures, which are displayed in Figure 33.

It is evident from the data that a regression is required to extrapolate the results to higher frequencies, as the original measurements do not extend to these ranges. To approximate the dielectric properties at these frequencies, we focus on the "Diluted Sweat" curve, representing a normally hydrated subject.

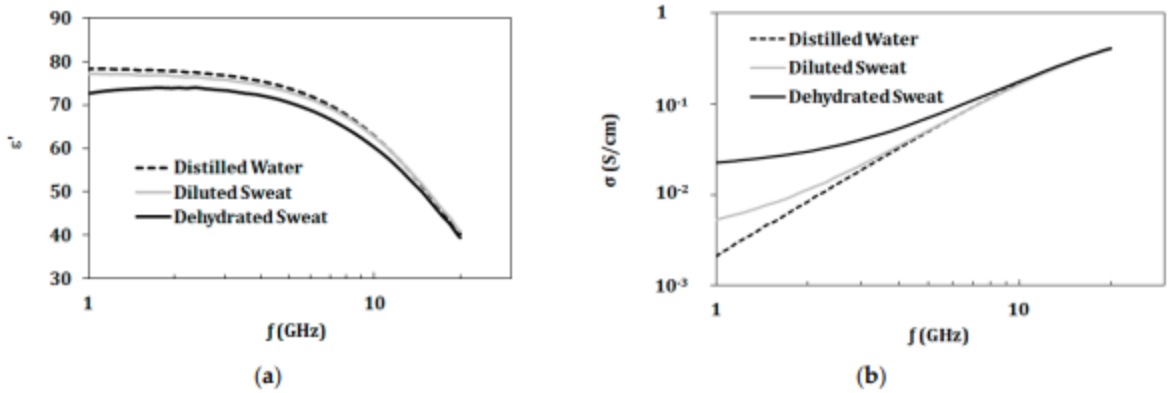

Figure 33: Dielectric constants for sweat at 26.5 GHz [35]

At 26 GHz, the real permittivity was around 23.20, with an imaginary component of 40 F/m, and a conductivity of 2 S/m, consistent with both studies. For the electrical conductivity, the value was 0.891 S/cm, equivalent to 8.915 x 10^{-3} S/m.

After characterizing the electromagnetic properties of human skin, the skin model was irradiated with plane waves of 1 V/m of amplitude and horizontal polarizations. Figure 34 shows the distribution of the electric field and joule heating across each layer of the skin model produced by a frontal plane wave polarized parallel and perpendicular to the arteriole central axis. In the figures, we can see that the case where the plane wave is parallel to the vessel axis produces higher fields and energy absorption.

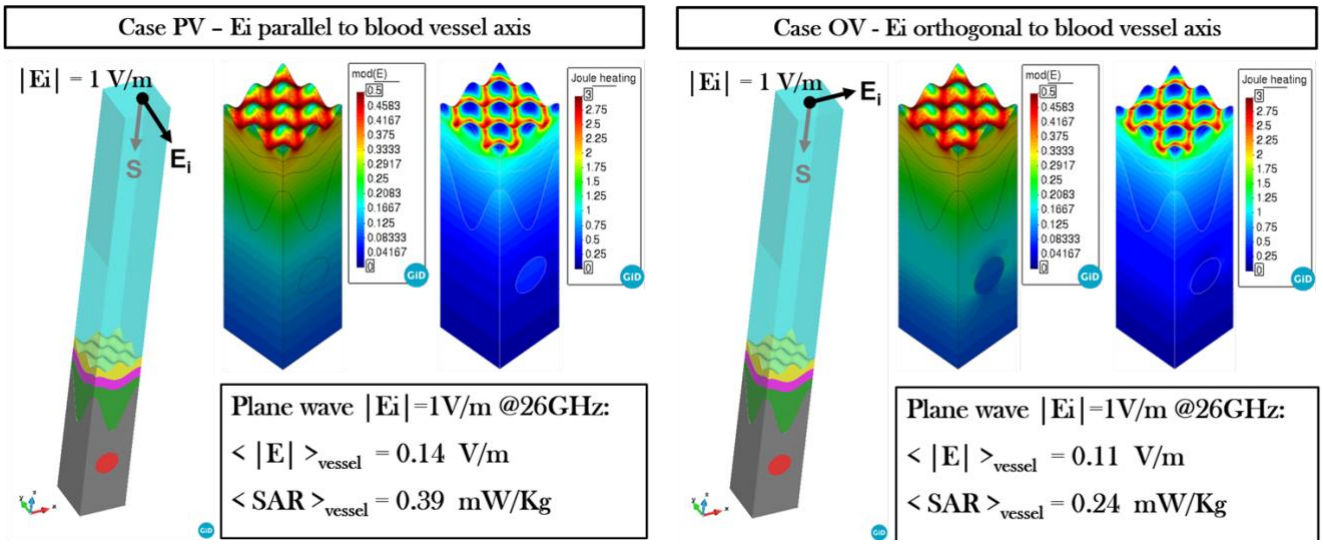

Figure 34: Electromagnetic field at 26 GHz for different polarization waves.

We observe that when the polarization of the electromagnetic field is aligned with the longitudinal axis of the arteriole, the SAR values are higher. This occurs because the alignment of the electric field with the vessel's axis enhances the coupling between the field and the conductive properties of the blood. When the electric field is parallel to the arteriole's axis, the effective exposure area increases, leading to more efficient energy transfer and higher absorption within the vessel. This phenomenon is a direct consequence of the field-tissue interaction, where the orientation of biological structures relative to the incident electromagnetic field significantly influences the absorption characteristics.

The worst-case scenario is shown in Figure 35: Case PV – Ei parallel to the blood vessel axis.

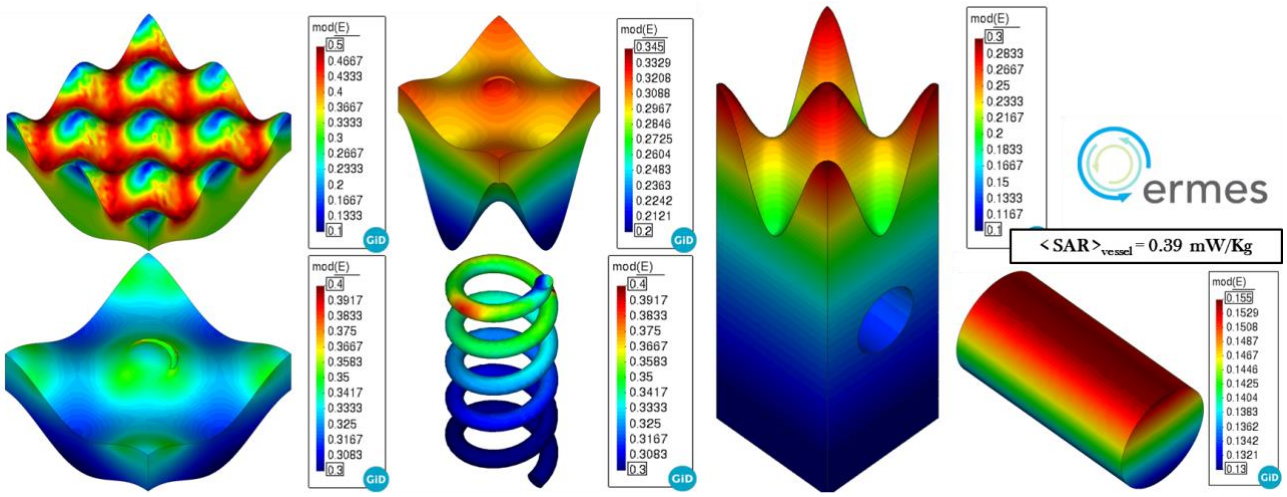

Figure 35: Electromagnetic field for the different layers at 26 GHz using ERMES.

5.2.2 Cross Validation

To validate the obtained results by ERMES (V.20), a cross-validation process was conducted using the commercial software CST Studio, specifically in the transient domain utilizing the Finite Integration Technique (FIT). This method ensures that the simulation results are accurate by comparing them with those obtained from a well-established numerical tool. CST Studio's FIT approach is widely recognized for its accuracy in solving Maxwell's equations in complex electromagnetic problems, especially when dealing with time-domain simulations. By employing this cross-validation, any discrepancies between ERMES and CST can be identified and addressed, further enhancing the reliability of the original simulation. Additionally, this comparison helps to verify that the electromagnetic field interactions and SAR distributions in the biological tissues are consistent across different computational platforms, providing confidence in the robustness of the model. Next image shows the results for each layer of the Skin model (Figure 36).

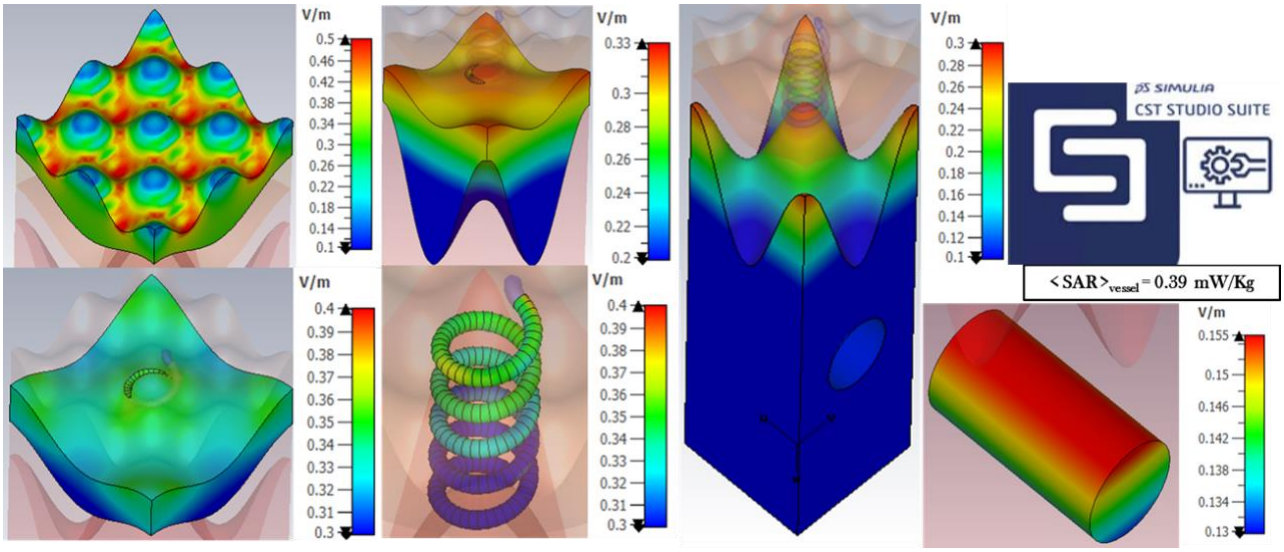

Figure 36: Electromagnetic field for the different layers at 26 GHz using CST Studio.

Next table show the computational mesh and simulation time for the human skin model at 26 GHz.

Table 8: Computational times for 26 GHz Simulations.

Code	Mesh	Time	Method	Hardware	OS
CST	**≈ 3.0e5 Hexahedral elements**	**≈ 20 min**	**Finite Integral Technique (FIT) Time Domain (TD)**	**Laptop: CPU: Intel(R) Core(TM) i7 750U @1.80 GHz, RAM: 32.0 GB**	**Win64**
ERMES	**≈ 3.6e5 1st order edge elements**	**≈ 2 min**	**Finite Element Method (FEM) Frequency Domain (FD)**	**Desktop: CPU: Intel(R) Core(TM) i5-10500 @3.10 GHz, RAM: 32.0 GB**	**Win64**
ERMES	**≈ 2.2e6 1st order edge elements**	**≈ 19 min**	**Finite Element Method (FEM) Frequency Domain (FD)**	**HPC cluster**	**Linux**

5.2.3 Simulations Coaxial probe at 26 GHz

A 3D model of the open-ended coaxial probe is being developed, with the final results to be presented in use case 3. The objective of this experiment is to validate the electromagnetic properties of the human skin model. The following image illustrates the experimental setup and the geometrical model used. To ensure that the numerical matching boundary does not excessively constrain the field distribution—which could potentially alter the probe's response and lead to discrepancies between the simulated and measured results—it is essential to define the diameter of the medium under test (MUT) to be approximately 2-3 times the size of the probe's dielectric gap. This approach helps to accurately replicate the interaction between the probe and the skin, minimizing boundary effects and ensuring that the simulation closely matches experimental conditions. The internal radius of the coaxial is 0.28 mm. The experiment will be performed up to 30 GHZ in order to cover the spectrum range.

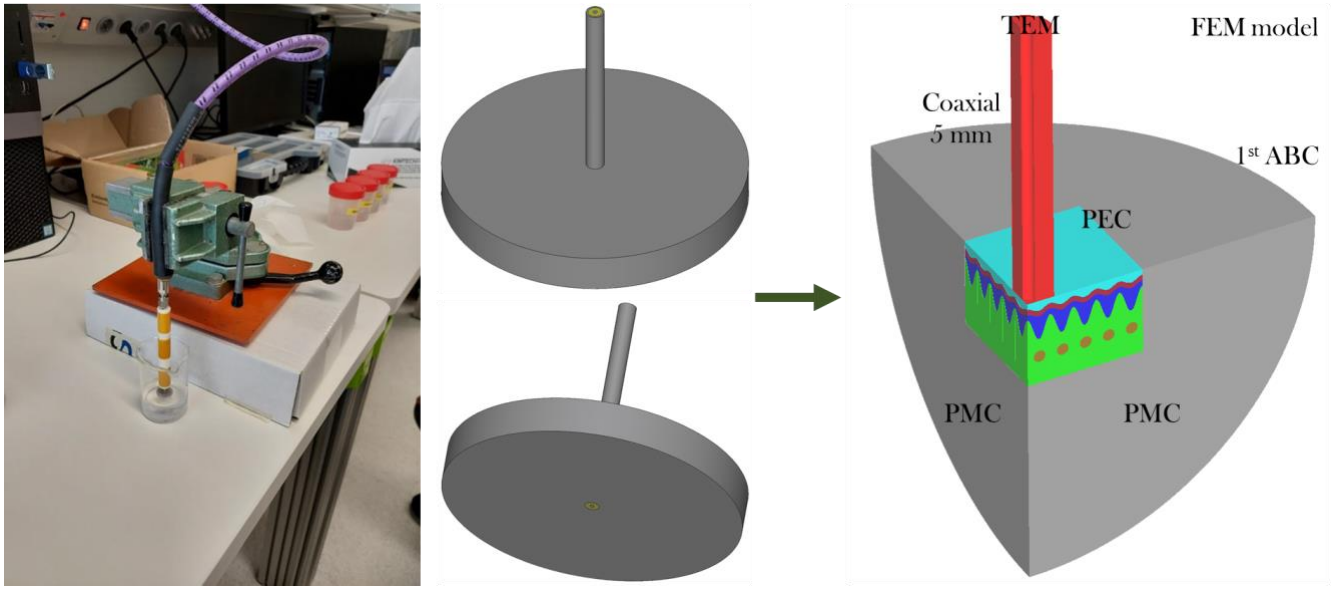

Figure 37: Experimental setup for the open-ended coaxial test.

The simulations with an open-ended coaxial probe at 3.5GHz and at 26 GHz for different material structure (vacuum, volume average, multi-layer, and a skin model) have been carried out. The color maps represent the electric field distribution (log scale of |E|), and the boxes below provide the reflection coefficient magnitude (|S11|) and phase values in radians for each scenario.

.

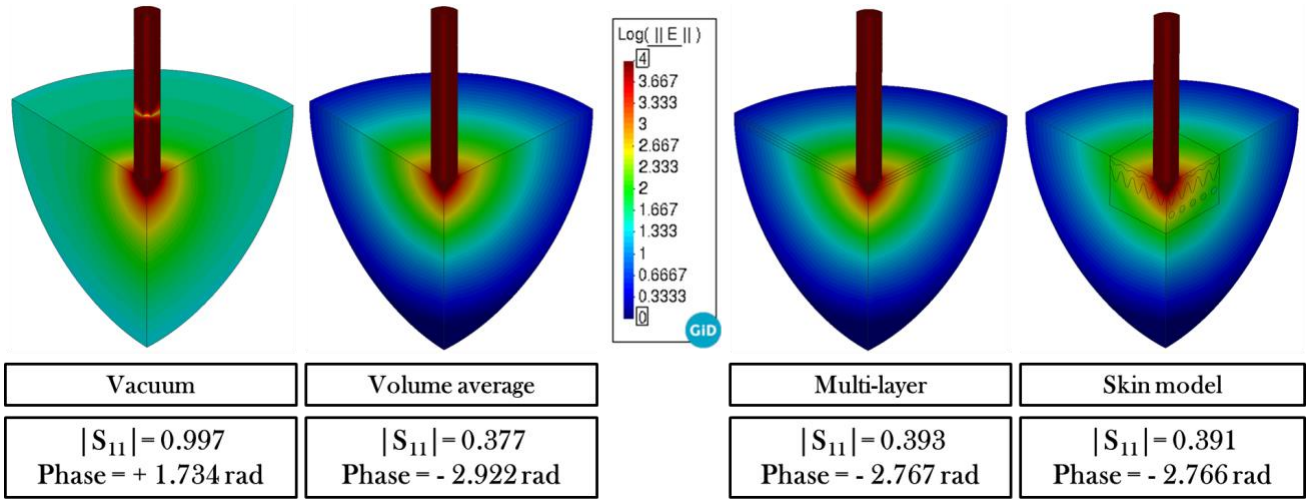

Figure 38:. Simulation results of an open-ended coaxial probe at 26 GHz for different test conditions and material models: vacuum, volume average, multi-layer, and a skin model.

In the first case, the probe is exposed to a vacuum. The reflection coefficient magnitude (|S11|) is very close to 1 (|S11| = 0.997), which indicates that almost all the electromagnetic energy is reflected to the probe. This is expected since there is no medium to absorb the energy. The phase shift is +1.734 rad, showing the phase difference of the reflected wave.

Volume Average: This simulation scenario we use a homogeneous dielectric material which properties has been obtained by volume average the properties of the skin model. The reflection coefficient magnitude drops significantly to |S11| = 0.377, suggesting more energy is being absorbed by the material compared to the vacuum case. The phase shift changes to -2.922 rad, indicating a larger phase delay due to the presence of the medium.

Multi-Layer: Here, the probe is placed over a multi-layer material, which represents a simplification of the skin model. Each layer has the same properties as its equivalent one in the skin model; the geometry is just different. This model was made to see how important the geometrical details are and to see if we can use simplified multilayer models for future simulations. The reflection coefficient magnitude is indeed very similar to the skin model, showing that it is a good approximation that can be used to reduce computational time.

Skin Model: In this scenario, a detailed skin model is used, representing the different layers of human skin, including the stratum corneum, epidermis, and dermis. The reflection coefficient magnitude is almost identical to the multi-layer case ($|S11| = 0.391$), implying that the skin model has a similar effect on energy absorption and reflection as the multi-layer structure. The phase shift is -2.766 rad, also very close to the multi-layer scenario, reflecting the complex interaction of the electromagnetic field with the layers of the skin.

This preliminary simulation highlights how different material properties (from vacuum to complex skin models) influence the electromagnetic field behavior around the coaxial probe at 26 GHz. The reflection coefficient ($|S11|$) and phase shift are critical parameters used to assess how much energy is absorbed by the material and how the material affects the phase of the electromagnetic wave. The skin model and multi-layer scenarios provide a realistic approximation of how the probe would behave when measuring biological tissues.

Following, a piece of human skin (10 x 5) (Figure 39) was simulated with an open-ended coaxial probe at 26 GHz.

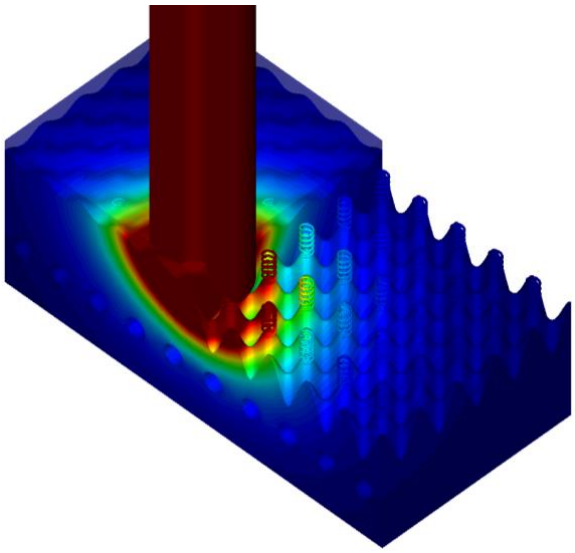

Figure 39: Simulation of an open-ended coaxial probe at 26 GHz for a full skin model.

A small measurement campaign is being performed to compare the results obtained by the simulations depicted in Figure 39 with average values in real skin measurements, see Figure 40. The data will be analyzed and compared with the model to eventually tune the dielectric skin properties in case study 3.

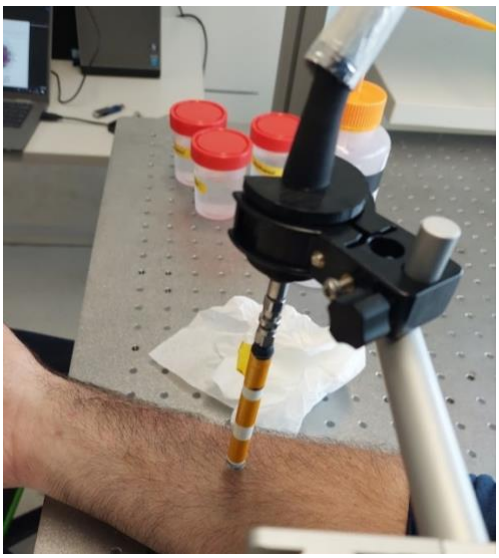

Figure 40: Measurement performed on skin tissue.

6 Conclusion

The primary objective of this deliverable was to outline the numerical models and methods employed in the NextGEM project to analyze the exposure and health effects of electromagnetic fields (EMFs) in the context of 5G and 6G technologies. The adoption of open-source electromagnetic codes, such as ERMES, enhanced the credibility of the research by providing a collaborative and transparent platform to explore, understand, and address the effects of EMFs. This approach was particularly relevant for emerging technologies like 5G and 6G, contributing to a robust knowledge base and offering reliable, informed answers, even to the most skeptical audiences.

This deliverable presented a range of simulation approaches, CAD models, and numerical tools that were developed or customized specifically for this project. It also provided preliminary examples of models and simulations across different scenarios and frequency ranges (FR1 and FR2). For the FR2 range, it was demonstrated that EMFs do not penetrate deeply into the body. Therefore, the modeling efforts focused on the body's surface, where boundary conditions were applied to simulate the interaction of EMFs with external space. This surface-focused approach allowed for the calculation of internal parameters, such as the average Specific Absorption Rate (SAR), and facilitated the assessment of EMF exposure and its potential impact on human health without requiring detailed volumetric modeling. This method proved to be both practical and efficient for analyzing EMF interactions at higher frequencies.

Examples of full-body surface models were provided in Sections 2.2 and 5.1 of this deliverable. Additionally, an overview of the geometric models used to represent the physical structures in the simulations, including volumetric and surface models, was included. It detailed the specific human body and skin models employed in the project.

Building on the content from Deliverable 3.2, this deliverable also included an in-depth analysis of a skin model for both FR1 and FR2 frequency ranges. Furthermore, a comparative study was conducted using different numerical codes, specifically ERMES and CST, to validate and reinforce the reliability of the obtained results. This comparison highlighted the robustness of the findings and underscored the importance of ensuring consistency across different simulation platforms.

As part of this deliverable, a preliminary study was also conducted using an open-ended coaxial cable probe. This technique was employed to measure the dielectric properties of biological tissues, such as skin, across different frequency ranges. The open-ended coaxial probe offered a non-destructive method for characterizing material properties in situ, making it particularly suitable for evaluating the electromagnetic behavior of tissues in the context of FR1 and FR2 frequencies. This study helped validate the electromagnetic properties of the skin model and provided crucial insights into how electromagnetic fields interact with biological tissues, particularly at the surface level, which is more relevant at the higher frequencies used in 5G and 6G technologies.

The inclusion of this comprehensive analysis added significant value to the deliverable, emphasizing the novel insights and methodologies introduced in this document.

References

[1] ICNIRP. Guidelines for limiting exposure to electromagnetic fields (100 kHz to 300 GHz). Health Phys 118(00):000–000; 2020. Pre-print. DOI: 10.1097/HP.0000000000001210.

[2] P. Sumithra and D. Thiripurasundari, "A review on computational electromagnetics methods," Advanced Electromagnetics, vol. 6, pp. 42-55, 2017.

[3] J. Mora, R. Otin, P. Dadvand, E. Escolano, M. A. Pasenau and E. Oñate, "Open tools for electromagnetic," The International Journal for Computation and Mathematics in Electrical and Electronic Engineering, vol. 25, no. 3, pp. 551-564, 2006.

[4] International Electrotechnical Commission. (2020). Measurement procedure for the assessment of specific absorption rate of human exposure to radio frequency fields from hand-held and body-mounted wireless communication devices – Human models, instrumentation and procedures (Frequency range of 300 MHz to 6 GHz). Geneva, Switzerland: IEC.

[5] Hwang, J. M. L., Shoup, R. L., Warner, G. G., & Poston, J. W. (1976). Mathematical descriptions of a one- and five-year old child for use in dosimetry calculations (No. ORNL/TM--5293). Oak Ridge National Lab.

[6] Cristy, M. (1980). Mathematical phantoms representing children of various ages for use in estimates of internal dose (No. NUREG/CR-1159; ORNL/NUREG/TM-367). Oak Ridge National Lab., TN (USA).

[7] Valentin, J. (2002). Basic anatomical and physiological data for use in radiological protection: reference values: ICRP Publication 89. Annals of the ICRP, 32(3-4), 1-277.

[8] Gosselin, M. C., Neufeld, E., Moser, H., Huber, E., Farcito, S., Gerber, L., ... & Kuster, N. (2014). Development of a new generation of high-resolution anatomical models for medical device evaluation: the Virtual Population 3.0. Physics in Medicine & Biology, 59(18), 5287.

[9] Makarov, S. N., Noetscher, G. M., Yanamadala, J., Piazza, M. W., Louie, S., Prokop, A., ... & Nummenmaa, A. (2017). Virtual human models for electromagnetic studies and their applications. IEEE reviews in biomedical engineering, 10, 95-121.

[10] Y. Feldman et al., "The electromagnetic response of human skin in the millimetre and submillimetre wave range," Phys. Med. Biol., vol. 54, no. 11, pp. 3341–3363, Jun. 2009.

[11] L. Gonzalez-Moragas, A. Roig, A. Laromaine,Adv. Col Intef. Sci, 291, 2015, 10-26, https://doi.org/10.1016/j.cis.2015.02.001

[12] R. Hiptmair, "Finite elements in computational electromagnetism," Acta Numerica, vol. 1, pp. 237-339, 2002.

[13] R. Otin, "ERMES: A nodal-based finite element code for electromagnetic simulations in frequency domain," Computer Physics Communications, vol. 184, no. 1, pp. 2588-2595, 2013.

[14] R. Otin, "Regularized Maxwell equations and nodal finite elements for electromagnetic field computations," Electromagnetics, vol. 30, no. 1-2, pp. 190-204, 2010.

[15] R. Otin, L. E. Garcia-Castillo, I. Martinez-Fernandez and D. Garcia-Donoro, "Computational performance of a weighted regularized Maxwell equation finite element formulation," Progress In Electromagnetics Research, vol. 136, pp. 61-77, 2013.

[16] J. Jin, The Finite Element Method in Electromagnetics, John Wiley & Sons, 2002.

[17] H. Duan, P. Lin and R. Tan, "Solving a Maxwell interface problem by a local L2 projected C0 finite element method," ENUMATH 2013 Lecture Notes in Computational Science and Engineering, vol. 103, 2015.

[18] R. Otin, "Numerical study of the thermal effects induced by a RFID antenna in vials of blood plasma," Progress In Electromagnetics Research Letters, vol. 22, pp. 129-138, 2011.

[19] R. Otin, J. Verpoorte, H. Schippers and R. Isanta, "A finite element tool for the electromagnetic analysis of braided cable shields," Computer Physics Communications, vol. 191, no. 1, pp. 209-220, 2015.

[20] R. Otin, R. Mendez and O. Fruitos, "A frequency domain approach for computing the Lorentz force in electromagnetic metal forming," International Journal of Applied Electromagnetics and Mechanics, vol. 46, no. 1, pp. 125-142, 2014.

[21] R. Otin, S. Aria, V. Thompson, R. Lobel, J. Willians, Z. Vizvary, D. Iglesias and M. Porton, "Computational electromagnetics for nuclear fusion engineering and design," NAFEMS Benchmark Magazine, 2020.

[22] "GiD: the universal, adaptive and user-friendly pre and post processor," International Centre for Numerical Mathods in Engineering (CIMNE), [Online]. Available: https://www.gidsimulation.com/. [Accessed 26 September 2023].

[23] "The 2-Clause BSD License - Open Source Initiative," Open Source Initiative, [Online]. Available: https://opensource.org/license/bsd-2-clause/. [Accessed 25 September 2023].

[24] R. Otin, "ERMES - Software," [Online]. Available: https://ruben-otin.blogspot.com. [Accessed 26 September 2023].

[25] T. B. A. Senior, "Impedance boundary conditions for imperfectly conducting surfaces," Applied Science Research, sec. B, vol. 8, pp. 418-436, 1960.
[26] T. B. A. Senior and J. L. Volakis, Approximate Boundary Conditions in Electromagnetics, IEE Press, 1995.
[27] S. Balay et al., "PETSc Web page," 2023. [Online]. Available: https://petsc.org/. [Accessed 26 September 2023].
[28] D. M. Pozar, Microwave engineering, John Wiley & Sons, Inc., 1998.
[29] Database of Dielectric Properties for Electromagnetic Modelling of Human Body. (2024). https://www2.nict.go.jp/cgi-bin/202303080003/public_html/index.py/measurements
[30] Institute for Applied Physics. (2024). Dielectric properties of Body Tissues. http://niremf.ifac.cnr.it/tissprop/htmlclie/htmlclie.php
[31] Sasaki, K., Wake, K., & Watanabe, S. (2014). Measurement of the dielectric properties of the epidermis and dermis at frequencies from 0.5 GHz to 110 GHz. Recuperado de https://pubmed.ncbi.nlm.nih.gov/25082800
[32] Malmiuvo, J., & Plonsey, R. (1995). Bioelectromagnetism. Principles and Applications of Bioelectric and Biomagnetic Fields.
[33] Lubangakene, I. D., Virdee, B., Karthick Rajaguru Jayanthi, R., & Ganguly, P. (2023). Effect of metabolite and temperature on artificial human sweat characteristics over a very wide frequency range (400 MHz–10.4 GHz) for wireless hydration diagnostic sensors.
[34] Raja Pavan, M. V., & Barron, A. R. (2022). Caracterización de permitividad eléctrica de soluciones acuosas
[35] Eldamak, A. R., Thorson, S., & Fear, E. C. (2020). Study of the Dielectric Properties of Artificial Sweat Mixtures at Microwave Frequencies. Biosensors (Basel), 10(6), 62.